High Hydrogen Content Syngas Fuel Burning in Lean Premixed Spherical Flames at Elevated Pressures: Effects of Preferential Diffusion

K.K.J. Ranga Dinesh [1*], H. Shalaby [1], K.H. Luo [2], J.A. van Oijen [3], D. Thévenin [4]

1. Energy Technology Research Group, Faculty of Engineering and the Environment, University of Southampton, Southampton SO17 1BJ, UK.

2. Department of Mechanical Engineering, University College London, Torrington Place, London WC1E 7JE, UK.

3. Combustion Technology Group, Department of Mechanical Engineering, Eindhoven University of Technology, Den Dolech 2, 5612 AZ Eindhoven, Netherlands.

4. Laboratory of Fluid Dynamics and Technical Flows, University of Magdeburg "Otto von Guericke", Universitatsplatz 2, D-39106 Magdeburg, Germany.

[*] **Corresponding Author**: K.K.J. Ranga Dinesh, Energy Technology Research Group, Faculty of Engineering and the Environment, University of Southampton, Southampton, SO17 1BJ, UK.

Email: Dinesh.Kahanda-Koralage@soton.ac.uk

Tel: +44 (0) 2380598301

Revised Manuscript Prepared for the Submission of International Journal of Hydrogen Energy

July 2016

Abstract

This study addresses the effects of preferential diffusion on flame structure and propagation of high hydrogen content (HHC) turbulent lean premixed hydrogen-carbon monoxide syngas flames at elevated pressures. The direct numerical simulations with detailed chemistry were performed in three-dimensional domain for expanding spherical flame configuration in a constant pressure combustion chamber. To identify the role of preferential diffusion on flame structure and propagation under low and high turbulence levels at elevated pressure, simulations were performed at an initial turbulent Reynolds number of 15 and 150 at a pressure value of 4bar. The results demonstrate that the thermo-diffusive instability greatly influences the lean premixed syngas cellular flame structure due to strong preferential diffusion effects under low turbulence level at elevated pressure. In contrast, the results reveal that the thermo-diffusive effects are destabilising and preferential diffusion is overwhelmed by turbulent mixing under high turbulence level at elevated pressure. This finding suggests that the development of cellular flame structure is dominated by turbulence with little or no contribution from the thermo-diffusive instability for the lean premixed syngas flame which operates under conditions of high turbulence and elevated pressures. However, results demonstrate that the flame acceleration and species diffusive flux are still influenced by the preferential diffusion for the lean premixed syngas flame which operates under conditions of high turbulence and elevated pressures.

Key Words: Direct Numerical Simulation, High Hydrogen Content Syngas Fuel, Elevated Pressures, Preferential Diffusion, Intrinsic Flame Instabilities

1. Introduction

The rapid increase of carbon dioxide (CO_2) emissions associated with fossil fuel combustion is compelling us to discover cleaner fuels and utilise them in next generation combustion devices for power generation and transportation [1]. The use of low carbon content fuels as a supplement for fossil fuels offers the advantage of a cleaner fuel without significantly changing the current combustion technologies and the associated massive infrastructure [2]. In this context, combustion of high-hydrogen content (HHC) synthesis gas (or syngas) fuels with a significant amount of hydrogen versus carbon monoxide is undoubtedly beneficial [3]. In particular, turbulent lean premixed combustion characteristics of HHC syngas fuel at elevated pressures is of both fundamental and practical importance to the design of the next generation clean and efficient combustion engines [4]. Unsurprisingly, there has been strong interest in the combustion community to investigate the fundamental characteristics of HHC syngas fuel burning in turbulent lean premixed combustion mode at elevated pressures [5-14].

Direct numerical simulation (DNS) of turbulent premixed flames has been a valuable technique in the investigation of the complex interactions between combustion and turbulence. Recently DNS simulations have added a great deal of understanding of many issues in turbulent premixed combustion benchmark problems [15-17]. Particularly, a large number of DNS studies on preferential diffusion effects on local flame structure, local flame propagation and pollutant emission formation of hydrogen and hydrogen-enriched hydrocarbon turbulent premixed flames at atmospheric pressure were reported in the literature. Preferential diffusion influences chemical reaction and heat transfer due

to high diffusivity of light chemical species such as H and H_2 that can play a significant role in hydrogen combustion [18]. It is often described by the Lewis number, Le, defined as the ratio of thermal to fuel mass diffusivities. For example, Im and Chen [19] investigated preferenatial diffusion effects on the burning rate of turbulent premixed hydrogen-air flames. Bell et al. [20] discussed the effect of Lewis number on flame morphology and local flame propagation speed on flame curvature in lean premixed hydrogen turbulent flame. Bisetti et al. [21] examined the effect of temperature stratitification on the occurence of preferential diffusion during the auto-ignition of lean premixed hydrogen-air mixture. In the same year, Dustan and Jenkins [22] and Vreman et al. [23] also reported preferential diffusion effects on hydrogen enriched methane flames in spherical and bunsen flame configurations respectively. Later, Aspden et al. [24, 25] repoted DNS results on the role of Lewis number in lean premixed hydrogen flame operating in the distributed burning regime. Wang et al. [26] have also reported preferential diffusion effects with respect to different equivalence ratio in hydrogen-air swirling premixed flames, while Kim et al. [27] studied the influence of preferential diffusion on downstream flame characterises of syngas flames. Luo et al. [28] have also analysed preferential diffusion effects on flame characteristics in turbulent premixed flames using DNS. In addition, DNS studies on preferential diffusion effects on flame structure and propagation of turbulent non-premixed flame characteristics at atmospheric pressure were also reported. For example, our earlier DNS work demonstrated that preferential diffusion greatly influences the flame structure, species mass fraction distribution and nitric oxide pollutant emission distribution in turbulent non-premixed syngas flames at atmospheric pressure [29-32].

Although these aforementioned DNS studies provide valuable insights into preferential diffusion effects on turbulent premixed flames at atmospheric pressure, DNS investigation of preferential diffusion effects on flame structure and propagation in turbulent premixed flame at elevated pressures has not been fully addressed in the past. Part of the problem is the lack of chemical kinetic mechanisms for HHC fuels at elevated pressures, so the majority of the mechanisms employed for DNS of lean premixed hydrogen or hydrogen-enrich syngas combustion have mainly been validated at atmospheric pressure. Only recent studies [33-36] have reported hydrogen and HHC syngas fuel chemical kinetic mechanisms at elevated pressures, which are yet to be applied to scrutinize the role of detailed chemical mechanisms in predicting key chemical species mass fractions in lean premixed syngas combustion at elevated pressures. Another issue is the practical difficulty of performing computationally expensive DNS with detailed chemistry at elevated pressures due to higher spatial and temporal resolution requirement. In view of the above consideration, we have performed three-dimensional DNS with a multistep detailed chemical reaction mechanism and the mixture-averaged transport model aiming at providing answer to the following key question: how does preferential diffusion (non-unity Lewis number) affect the flame structure, onset of instability, flame speed, and species mass diffusion for lean premixed H_2/CO syngas flames which operate under conditions of low initial turbulence and high initial turbulence respectively at elevated pressure?

In the context of experimental investigation of flame structure and propagation of turbulent premixed combustion at elevated pressures, centrally-ignited outwardly

propagating (expanding spherical) flame has been studied extensively, for example see [6-9] [37, 38]. In this work, we attempt to find answer to the question raised above based on DNS of centrally-ignited expanding lean premixed turbulent HHC syngas flames. Three sections will follow. The next section describes the mathematical and numerical details of the DNS as well as the chemical mechanisms and diffusion models. Section 3 describes the key results, followed by conclusions in section 4.

2. Mathematical Formulation and Numerical Computation

2.1 Governing equations, Chemistry and Diffusion Model

The full compressible governing equations together with considered thermodynamical relations, chemistry and transport models are solved using the parallel DNS flame solver, Parcomb [39, 40]. Using the Cartesian tensor notation and ignoring all external forces, the conservation equations solved in DNS read:

Mass conservation:

$$\frac{\partial \rho}{\partial t} + \frac{\partial (\rho u_j)}{\partial x_j} = 0 \tag{1}$$

Momentum conservation:

$$\frac{\partial (\rho u_i)}{\partial t} + \frac{\partial (\rho u_j u_i)}{\partial x_j} = -\frac{\partial p}{\partial x_i} + \frac{\partial \tau_{ij}}{\partial x_j}; \quad i = 1,2,3 \tag{2}$$

Species balance:

$$\frac{\partial (\rho Y_i)}{\partial t} + \frac{\partial \left[\rho (u_j + V_{ij}) Y_i \right]}{\partial x_j} = \dot{\omega}_i; \quad \mathrm{i} = 1, N_s \tag{3}$$

Energy conservation:

$$\frac{\partial(\rho e_t)}{\partial t} + \frac{\partial\left[(\rho e_t + p)u_j\right]}{\partial x_j} = -\frac{\partial q_j}{\partial x_j} + \frac{\partial(\tau_{ij}u_j)}{\partial x_i} \tag{4}$$

Equation of state:

$$\frac{p}{\rho} = \frac{R}{\overline{W}}T \tag{5}$$

In Eqs. (1-5), t stands for time, ρ the mixture density, u_j velocity components in the x_j direction, τ_{ij} stress tensor, e_t total energy per unit mass, p pressure, Y_i the mas fraction of species i, N_s the total number of species, V_{ij} the component of the diffusion velocity of species i in the direction j, $\dot{\omega}_i$ the chemical production rate of species i, q_j the jth-component of the heat flux vector, R the perfect gas constant ($R = 8.314\ \text{Jmol}^{-1}\text{K}^{-1}$) and $\overline{W}$ is the mixture-averaged molar mass.

In this investigation we have employed a H_2/CO kinetic scheme developed and validated at elevated pressure by Goswami et al. [35, 36]. This reaction model incorporates the thermodynamic, kinetic, and species transport properties related to elevated pressure H_2 and CO oxidation, consisting of 14 species (O, O_2, N_2, H, H_2, H_2O, OH, H_2O_2, HO_2, CO, CO_2, HOCO, HCO, and CH_2O) and 52 individual reactions. In this study, we employed the mixture-averaged transport model supplemented with a model for Soret effect (thermal diffusion) to compute the diffusive process. To compute the diffusion velocity of species i in the mixture, the following formulation is used:

$$\boldsymbol{V}_i = -\sum_{k=1}^{N_s} D_{ik}\boldsymbol{d}_k - D_i^T \frac{\nabla T}{T} \tag{6}$$

In Eq. (6), D_{ik} denotes the multi-species diffusion coefficient matrix of species i into species k which depends on all state variables. The mass conservation constraint for the species diffusion velocities reads $\sum_{i=1}^{N_s} Y_i \mathbf{V}_i = 0$. $\mathbf{d}_k$ is a species diffusion driving force vector that takes into account gradients of mole fraction and pressure. In most cases, as in the present study, the pressure-induced diffusion is negligible and the external forces $\mathbf{f}_j$ are considered to act equally on all species, resulting simply in $\mathbf{d}_k = \nabla X_k$. D_i^T is the thermal diffusion coefficient of species i while the combined term $D_i^T \nabla T / T$ is the Soret or thermodiffusive effect, which accounts for the diffusion of mass as a result of temperature gradient. Soret effect tends to drive light molecules towards hot regions and heavy molecules towards cold region of the flow. It is important to note that Soret effect is considered to be vital in situations where light radicals such as H or H_2 are present, in particular for HHC syngas combustion. To compute the diffusion velocities, one has to accurately determine the binary coefficient via the diffusion matrix, which is computationally expensive. In this study, we consider the Hirschfelder-Curtiss approach [41], whereby an appropriate diffusion coefficient, D_i^* for the species i is given as

$$D_i^* = \frac{(1-Y_i)}{\sum_{k=1,k\neq i}^{N_s} (X_i / D_{ik})} \tag{7}$$

where D_{ik} is the binary diffusion coefficient which depends only on species pair properties, pressure and temperature and X_i is the mole fraction of species i. The

diffusion velocity $\mathbf{V}_i$ for species i is divided into a predictor ($\mathbf{V}_i^*$) and a corrector ($\mathbf{V}_c$) term in order to satisfy the mass conservation, which leads to:

$$\boldsymbol{V}_i = \boldsymbol{V}_i^* + \boldsymbol{V}_c; \quad \boldsymbol{V}_i^* = -D_i^* \frac{\nabla X_i}{X_i} - D_i^* \chi_i^* \frac{\nabla T}{T}; \quad \boldsymbol{V}_c = -\sum_{k=1}^{N_s} Y_k \boldsymbol{V}_k^* \tag{8}$$

where χ_i^* is the thermal diffusion ratio.

Alternatively, for unity Lewis number calculations, each species is considered to have the same diffusion coefficient as heat, and the diffusion coefficient for species i is expressed as:

$$D_i = \frac{\lambda}{\rho C_P} \tag{9}$$

where λ is the mixture-averaged thermal conductivity and C_P the mixture specific heat capacities at constant pressure.

2.2 Numerical Computation

The expanding spherical flame is adopted as a model flame for the present investigation. In all the considered cases, three-dimensional DNS were performed for HHC lean premixed H_2/CO syngas fuel mixture with 70% of H_2 and 30% of CO by volume with an equivalence ratio of 0.7. It is believed that the preferential diffusion effects should play a role in stoichiometric premixed HHC syngas mixtures. However, it is also believed that the preferential diffusion reduces or diminishes for rich mixtures particularly at higher initial turbulence levels. Therefore we focused on the lean mixture where preferential diffusion is expected to play a greater role compared to stoichiometric and rich mixture under low and high turbulence levels respectively at elevated pressure.

To investigate the preferential diffusion effects on flame structure and propagation under low and high turbulence levels at elevated pressure, four DNS test cases were performed. Two simulations, one with non-unity Lewis number and another with unity Lewis number were performed at lower initial turbulent Reynolds number of Re_t=15, and at pressure value of p=4bar. Another two simulations, one with non-unity Lewis number and another with unity Lewis number were performed at higher initial turbulent Reynolds number of Re_t=150, and at pressure value of p=4bar. All turbulence properties as well as numerical parameters based on conditions at the beginning of the simulation are listed in Table 1.

The cubic domain has a length of 8.0×10^{-3}m on each side (Fig.1). A time step of approximately 6.0×10^{-9}s was used for all simulations. The governing equations are discretised in space on a three-dimensional Cartesian grid with high-order finite difference numerical schemes. Derivatives are computed using centered explicit schemes of order six except at boundaries where the order is progressively reduced to four. Temporal integration is realized with a Runge–Kutta algorithm of order four. A Courant-Friedrichs-Levy (CFL) condition for the convective terms and a Fourier condition pertaining to the diffusion terms are treated to ensure the stability of the explicit integration and determine a suitable time step. To maintain the constant pressure throughout the simulation, boundary conditions are treated with the help of improved non-reflecting inflow/outflow Navier-Stokes characteristics boundary condition (NSBC) by considering additional terms in the definition of the wave amplitudes, and the relaxation treatment for the transverse gradient terms in analogy with the pressure

relaxation [42]. The homogeneous isotropic turbulent velocity field for each case was initialised using a combined approach of digital filtering (DF) [43] and random noise diffusion [44]. The initial laminar spherical flame is constructed at the center of the computational domain with initial radius of $r_0 = 0.6\text{mm}$. The initial profiles of temperature and mass fractions of species is then prescribed according to:

$$\phi = \phi_0 + \frac{\Delta\phi}{2}\left[1 - \tanh\left(k.\left(\frac{r - r_0}{r_0}\right)\right)\right] \tag{10}$$

Here $\Delta\phi$ is the variation between the initial approximate values in the fresh and burnt gas mixture and real number k is a measure of the stiffness at the fresh/burnt gas interface (here, k=10.0). The flame thickness δ_{th} is evaluated as

$$\delta_{th} = \frac{T_b - T_u}{\max|\nabla T|}, \tag{11}$$

where T_u and T_b are the fresh and burnt gas temperatures, respectively. An initial temperature of $T_u = 300\text{K}$ is used. From the calculation of turbulence intensity u'/S_L and length-scale ratio l_t/δ_{th}, it can be concluded that the flames considered here fall mainly within the Thin Reaction Zone.

To gain an understanding of the effect of grid resolution on the DNS results at elevated pressures, simulations were conducted using four different grids at pressure value of p=4bar and turbulent Reynolds number of Re_t=150. The resolutions used for four different uniform Cartesian grids are $200\times200\times200$, $400\times400\times400$, $600\times600\times600$ and $800\times800\times800$ points in x, y and z directions respectively. Fig. 2 shows the comparisons of temporal evolution of the

integrated heat release rate and the spatial variation of the chemical production rate of hydrogen species obtained from four different grid resolutions for the expanding spherical flame at p=4bar and Re_t=150. Particularly, comparisons of temporal evolution of the integrated heat release rate and the spatial variation of the chemical production rate of hydrogen species show strong discrepancy between $200\times200\times200$ and $400\times400\times400$. These two simulations detected numerical wiggles for spatial distribution of the chemical source term of hydrogen species. They also show misalignment for the temporal evolution of the integrated heat release rate. However, Fig. 2 (a) and (b) show the comparisons between $600\times600\times600$ and $800\times800\times800$ for temporal evolution of the integrated heat release rate and the spatial variation of the chemical production rate of hydrogen species are remarkably consistent. Therefore, overall results obtained from four different grids indicate that a Cartesian grid with $600\times600\times600$ grid points produces grid independent results for the expanding spherical flame at Re_t=150, and at p=4bar.

We also employed several parameters for the post-processing calculation. To describe the local chemical state between unreacted and fully reacted mixture, we define the non-dimensional progress variable:

$$c=\frac{T-T_u}{T_b-T_u}=\begin{cases}0 & \text{fresh gas mixture}\\ 1 & \text{burnt gases}\end{cases} \tag{12}$$

where T_u and T_b are the unburned and burned gas temperatures, respectively. For the purpose of evaluating strain rate and curvature effects, the tangential strain rate and curvature are also defined. Here, the tangential strain rate is given by:

$$a_T = (\delta_{ij} - N_i N_j) \left. \frac{\partial u_i}{\partial u_j} \right|_{c=c^*}, \tag{13}$$

where N_i is the ith component of the local flame normal vector, given by:

$$N_i = -\frac{1}{|\nabla c|} \frac{\partial c}{\partial x_i} \tag{14}$$

The local curvature was calculated from the flame front coordinates using the following formula:

$$\kappa = \left. \frac{\partial N_i}{\partial x_i} \right|_{c=c^*}, \tag{15}$$

where κ is taken to be positive (negative) when the flame is convex (concave) in the direction of the unburned mixture.

Flame stretch is a measure of surface deformation and defined as:

$$\mathrm{k} = \frac{1}{A} \frac{dA}{dt}, \tag{16}$$

where k is the stretch, A is an element of flame area and t is time. The element of area is defined by points on the flame surface moving at the local tangential velocity and combined effects of curvature $\kappa = \nabla \cdot \mathbf{n}$ and hydrodynamic strain $\mathrm{K_s} = -\mathbf{n} \cdot \mathbf{a}_\mathrm{T} \cdot \mathbf{n}$, where $\mathbf{a}_\mathrm{T}$ is the strain rate tensor, and unit normal vector $\mathbf{n} = \nabla \mathrm{c} / |\nabla \mathrm{c}|$. Therefore the stretch rate k can be written as:

$$\mathrm{k} = \kappa S_d + \mathrm{K}_s. \tag{17}$$

where S_d is the flame displacement speed.

3. Results and Discussion

In discussing the DNS results, we examine the role of preferential diffusion on cellular flame structure and propagation, the onset of flame instability and the species diffusion flux under low turbulence and elevated pressure conditions, and high turbulence and elevated pressure conditions respectively. For this, we compare cellular flame structures, flame acceleration, onset of intrinsic flame instabilities and chemical species diffusion between the flame with non-unity Lewis number and the flame with unity Lewis number under low and high turbulence levels at elevated pressure.

3.1 Development of Cellular Flame Structures

According to the literature, lean premixed flames, and high hydrogen content fuel-air mixtures in particular, are subjected to two major types of cellular flame instabilities at elevated pressures: thermo-diffusive (TD) instability and Darrieus-Landau (DL) hydrodynamic instability [9, 37]. Thermo-diffusive instability arises due to an imbalance between chemical and sensible enthalpy fluxes from the reaction zone as a result of preferential diffusion (non-unity Lewis number) effects, while Darrieus-Landau instability occurs as a consequence of the gas thermal expansion (density ratio between the two sides of the flame front). Although it is widely believed that the thermo-diffusive instability and the Darrieus-Landau instability are of the utmost important for lean premixed flames, the buoyant instability can also be occurred in lean premixed spherical flames which is commonly regarded as be relevant to body-force [45]. Concerning the effect of buoyancy, it can play a role, especially since buoyant forces increase with increasing pressure, as well as with flame size. However, if the characteristic time for flame propagation is much smaller than that for buoyant convection, then the effect of

gravity should be small, as is the case for the syngas mixture in the equivalence ratio, flame radius, and pressure examined.

In order to distinguish the role of preferential diffusion on cellular flame wrinkling and the onset of instabilities, results from four different simulations were analysed at pressure value of p=4bar: Re_t=15 (unity Lewis number flame and non-unity Lewis number flame), and Re_t=150 (unity Lewis number flame and non-unity Lewis number flame). Figs. 3 and 4 show the temporal evolution of three-dimensional iso-contours of flame front temperature (T=1240 K, c=0.5) for flames with unity and non-unity Lewis numbers for the weak turbulence case (Re_t=15) and for the strong turbulence case (Re_t=150) at pressures value of p=4bar. It is seen that, at Re_t=15, and at p=4bar, the flame surface is wrinkled almost immediately after initiation of propagation for the non-unity Lewis number flame compared to the unity Lewis number flame. In particular, zoom view images of spherical flames in Fig. 3 indicate that the flame with non-unity Lewis number exhibits more small scale cells compared to the flame with unity Lewis number. This observation demonstrates that flame wrinkling is influenced by small scale cellular cells associated with instabilities for the flame which operates under conditions of low turbulence and elevated pressure.

It can be seen from Fig. 3 that flame with non-unity Lewis number and flame with unity Lewis number display large scale wrinkling structures, possibly due to DL instability as a result of the gas thermal expansion under low turbulence level at elevated pressure. However, the appearance of small scale cells indicates that the intensity of destabilisation

is particularly strong for the flame with non-unity Lewis number as a direct consequence of the TD instability due to preferential diffusion effects. This visualisation confirms that the development of cellular burning structures is influenced by the TD instability via preferential diffusion effects for the lean premixed syngas flame which operates under conditions of low turbulence and elevated pressure.

In contrast to observation made in Fig. 3, the clear observation from Fig. 4 is that the development of cellularity is almost identical for the flame with non-unity Lewis number and the flame with unity Lewis number for the strong turbulence case with Re_t=150 at pressure value of p=4bar. Furthermore, zoom view images shown in Fig. 4 also display very similar wrinkling structures for the two flames under high turbulence and elevated pressure. This observation indicates that the development of cellular flame structures in these two flames are greatly influenced by strong turbulence initially imposed in simulations. Therefore based on the observations made in Figs. 3 and 4, it is reasonable to expect that the evolution of flame wrinkling under high turbulence and elevated pressure is predominantly dominated by turbulence mixing which should be much faster than molecular mixing. The thermo-diffusive and the hydrodynamic contribution to overall instability will be discussed in the next section.

To gain an understanding of preferential diffusion effects on local curvature for flames develop under low and high turbulence levels at elevated pressure, we plotted the iso-surfaces of flame front coloured by curvature values at the flame front (T=1240K, c=0.5). Fig. 5 shows iso-surfaces of flame front coloured by local curvature for simulated flames.

The three-dimensional structures of local curvature in Fig. 5 (top) shows more local regions of positive higher curvature zones for the flame with non-unity Lewis number compared to the flame with unity Lewis number for the weak turbulence case. In contrast, Fig. 5 (bottom) shows almost identical curvature distribution for the flame with non-unity Lewis number and the flame with unity Lewis number for the strong turbulence case. It is noted that the positive curvature values (those part of the flame that are convex to the unburned gas) enlarge the flame front, while negative curvature values (those part of the flame that are concave to the unburned gas) contract the flame front. The observed trends in Fig. 5 demonstrate that local flame curvature is greatly influenced by the preferential diffusion affects for the lean premixed syngas flame which operates under conditions of low turbulence and elevated pressure.

To further assess the influence of preferential diffusion on flame front wrinkling under low and high initial turbulence levels at elevated pressure, we analyse the flame surface area. For this, we compare the flame surface area (surface area is calculated at an iso-surface of c=0.5) at a given radius between the flame with non-unity Lewis number and the flame with unity Lewis for the weak and strong turbulence cases at p=4bar. As seen in Fig. 6, results demonstrate that the flame surface area is much lager for the flame with non-unity Lewis number compared to the flame with unity Lewis number for the flame develops under conditions of low turbulence and elevated pressure. In contrast, Fig. 6 also shows nearly identical values for the surface area between the flame with non-unity Lewis number and the flame with unity Lewis number for the flame which develops under conditions of high turbulence and elevated pressure. Note that since the

characteristics of turbulence such as intensity and length scale do not change much during the early phase of evolution in high turbulence, both spherical flames undergo quite similar turbulence and hence, the flame surface areas for the two cases exhibit nearly identical values at the same radius regardless of the time.

3.2 Darrieus-Landau Instability, Thermo-Diffusive Instability and Growth Rate

To further assess the onset of instabilities on the response of preferential diffusion, one can analyse the DNS data combining with the linear stability theory. As such, the influence of preferential diffusion on the TD instability can be adequately compared under low and high turbulence levels at elevated pressure. In this sense, we calculate the contribution of the TD instability and the contribution of the DL instability on the growth rate for simulated flames using the linear stability theory originally developed by Bechtold and Matalon [46] and later reconstructed and extended by Bradley [47, 48]. The focus here is to isolate the preferential diffusion effects on overall flame instabilities for low and strong turbulence flames at elevated pressure by analysing non-unity and unity Lewis number results at Re_t=15 and Re_t=150, and at elevated pressure value of p=4bar.

Following Bradley's [47, 48] derivations, we computed the growth rate, $\omega(1-\Omega/Pe)$, contribution to the growth rate of the DL instability, ω, and contribution to the growth rate of the TD instability, $-\omega\Omega/Pe$. It is important to note that mathematical expressions for the growth rate, DL and TD instabilities in terms of series of spherical harmonic integers, n, are given here with modified expressions reported by Bradley [48]:

$$\omega = \frac{-(b-a) + \sqrt{((b-a)^2 - 4ac)}}{2a} \tag{18}$$

$$\Omega = \frac{Q_1 + lQ_2}{\omega} \tag{19}$$

Where

$l = \dfrac{\beta(Le_{eff} - 1)}{(\sigma - 1)}$ represents the deviation of effective Lewis number from unity,

$$a = (\sigma + 1)n + 1 \tag{20}$$

$$b = 2n^2 + (4 + 5\sigma)n + 4 \tag{21}$$

$$c = -\frac{(\sigma - 1)n^3}{\sigma} + 2n^2 + \left[3(\sigma + 1) - \frac{1}{\sigma}\right]n + 2 \tag{22}$$

$$Q_1 = \left[2\omega a + b - 2a\right]^{-1} \left\{ \begin{array}{l} \dfrac{\ln \sigma}{\sigma - 1}[(\sigma + 1)n^4 + (2\omega + 5)\sigma n^3 + (\omega\sigma - 2\sigma^2 + \sigma - 1)n^2 \\ +(\sigma - 7 - 3\omega - \sigma\omega)n\sigma - 2\sigma(1 + \omega)] + n(n^2 - 1)(n + 2)\dfrac{\sigma - 1}{\sigma} \end{array} \right\} \tag{23}$$

$$\begin{aligned} Q_2 = \gamma \left[2\sigma(2\omega a + b - 2a)\right]^{-1} \{ & 2n^4 + [2\omega\sigma + 2\omega + 10\sigma - 3]n^3 \\ & + [2\sigma\omega^2 + (5\sigma - 1)\omega + 3\sigma - 2\sigma^2 - 2]n^2 \\ & + [\sigma\omega^2(1 - 4\sigma) - (14\sigma^2 + 1)\omega + 3 - 9\sigma - 8\sigma^2]n - 2\sigma(\omega^2 + 4\omega + 3)\} \end{aligned} \tag{24}$$

$\sigma(=\rho_u / \rho_b)$ is the thermal expansion parameter, $Pe(=r/\delta_l)$ the Peclet number, $\beta(=T_a(T_b - T_u)/T_b^2)$ the Zeldovich number, $\gamma = \sigma \int_1^{\sigma} (\ln(s)/(s-1))ds$, Le_{eff} the effective Lewis number. Here r is the flame radius, δ_l the flame thickness, suffices u and b indicate unburned and burned gas and T_a the activation temperature.

Since we have two fuels (H_2 and CO) in the syngas mixture, the fuel Lewis number of the reactant is evaluated using the method proposed by Law et al. [37]:

$$Le_{H_2/CO} = 1 + \frac{q_{H_2}(Le_{H_2} - 1) + q_{CO}(Le_{CO} - 1)}{q_{H_2} + q_{CO}} \tag{25}$$

where $q_i = QY_i / C_P T_u$ (i refers to H_2 and CO) is the non-dimensional heat release associated with the consumption of species i, Q is the heat of reaction and Y_i is the supply mass fraction of species i. $Le_{H_2}(\approx 0.317)$, $Le_{CO}(\approx 1.171)$ are the fuel Lewis numbers of H_2-air mixture at ϕ_{H_2} and CO-air mixture at ϕ_{CO} respectively, where $\phi_{H_2} = (n_{H_2} / n_A)/(n_F / n_A)_{st}$, $\phi_{CO} = (n_{CO} / n_A)/(n_F / n_A)_{st}$ are the hydrogen and carbon monoxide-based equivalence ratio respectively, $n_{H_2}, n_{CO}, n_F, n_A$ are the mole fractions of hydrogen, carbon monoxide, fuel and air in the reactant mixture.

Since our primary goal is to assess the preferential diffusion effects on the onset of TD and DL instabilities and growth rate of H_2/CO syngas flame under low and high turbulence levels at elevated pressure, we employed a recently developed model equation for an effective Lewis number with information available from the flow field [49]. An important benefit of this model is that it allows us to assess the influence of turbulence on the effective Lewis number. It basically describes the transition from laminar Lewis number to unity effective Lewis number if the turbulence is sufficiently intense. The model equation for the effective Lewis number Le_{eff} can be expressed as

$$Le_{eff} = \frac{1 + a^{RANS}\,\mathrm{Re}_T}{\dfrac{1}{Le_{H_2/CO}} + a^{RANS}\,\mathrm{Re}_T} \tag{26}$$

where Re_T is the turbulent Reynolds number. Savard and Blanquart [49] reported that the parameter a^{RANS} can be varied between 0.1-0.2. The results presented in this paper used the value of $a^{RANS} = 0.1$. We also checked the results with $a^{RANS} = 0.2$ and found that the results are qualitatively similar to $a^{RANS} = 0.1$.

Shown in Figs. 7 and 8 are the contribution to the growth rate of the TD instability, $-\omega\Omega / Pe$, contribution to the growth rate of the DL instability, ω, and the growth rate, $\omega(1-\Omega / Pe)$ as a function of wave number for flames with unity and non-unity Lewis numbers at Re_t=15 and Re_t=150, and at pressures value of p=4bar. For the H_2/CO syngas mixture with 70% H_2 and 30% CO in the fuel mixture, the calculated Lewis number of the syngas mixture, $Le_{H_2/CO}$ using Eq. (25) at pressure value of p=4bar is 0.385. The thermal expansion parameter, $\sigma = 6.8$ and the Zeldovich number, $\beta = 8.0$. Here the value of the Zeldovich number β was chosen based on the minimum ignition energy of the non-uniform lean premixed syngas mixture. The Peclet number *Pe* for the weak turbulence flame with Re_t=15 is 303, while its value for strong turbulence case with Re_t=150 is 435. The effective Lewis number Le_{eff} obtained from the Eq. (26) for Re_t=15 and Re_t=150 are 0.61 and 0.91 respectively.

The observation from Fig. 7 is that the TD instability parameter, $-\omega\Omega / Pe$, shows large differences between the flame with non-unity Lewis number and the flame with unity Lewis number for the weak turbulence case at pressure value of p=4bar. In Fig. 7, the TD contribution to instability shown by the solid curve, is positive for all values of n, thus

indicates the onset of TD instability as a result of strong preferential diffusion effects for the lean premixed non-unity Lewis number flame which operates under conditions of low turbulence and elevated pressure. In contrast, the TD instability plot in Fig. 8 indicates that the TD effects are stabilising for the non-unity Lewis number flame which operates under conditions of high turbulence and elevated pressure. This finding further confirms that the TD instability does not develop for the flame with strong initial turbulence at elevated pressure, and it is overwhelmed by turbulence mixing. Meanwhile for $Le = 1.0$, TD contribution to instability shown by the broken curve is negative irrespective of the flow being weak or strong turbulence thus indicates the TD effects are stabilising for the flame with unity Lewis number.

The DL instability parameter ω, depends solely on the thermal expansion coefficient σ, which has a value of 6.8 for the flame with non-unity Lewis number and the flame with unity Lewis number in our calculations. Therefore, the contribution to the growth rate of the DL instability is found to be equal for both flames irrespective to the effects of preferential diffusion. Furthermore, the positive values of the DL instability parameter, ω, suggests that the DL influence is destabilising hence confirm the existence of the DL instability. The growth rate parameter, $\omega(1-\Omega/Pe)$, shows positive value for the flame with non-unity Lewis number and negative values for the flame with unity Lewis number for the weak turbulence case (Re_t=15). However, it shows negative values for the flame with non-unity Lewis number and the flame with unity Lewis number for the strong turbulence case (Re_t=150).

3.3 Flame Speed

To assess the preferential diffusion on flame acceleration under high turbulence and elevated pressure, we next compute the response of preferential diffusion on the local flame displacement speed (i.e., flame front speed relative to the flow) [50, 51] at Re_t=150, and at p=4bar. We investigate how the local flame displacement speed varies with flame stretch between the flame with non-unity Lewis number and the flame with unity-Lewis number at Re_t=150, and at p=4bar. We calculate the flame displacement speed for expanding spherical flames with and without preferential diffusion at Re_t=150, and at p=4bar and plot against the local stretch rate on the iso-surface in the preheat zone, reaction zone and fully burned zone. The flame displacement speed, which measures the difference between the flame front speed and the flow speed, is computed using the following expression [50, 51]:

$$S_d = \frac{1}{\rho C_P |\nabla T|}\left[\dot{\omega}_T' + \frac{\partial}{\partial x}\left(\lambda \frac{\partial T}{\partial x_i}\right) - \frac{\partial T}{\partial x}\left(\rho \sum_{i=1}^{N} C_{p,i} Y_i V_i\right)\right]. \quad (27)$$

where all the terms are evaluated along the selected isotherms. In Eq. (27), the first, second and third terms represent the effect of the heat release rate, energy transfer by conduction and energy transfer by diffusion fluxes through the different species respectively.

Fig. 9 shows the joint probability density function (JPDF) of the flame displacement speed and stretch rate for flames with non-unity Lewis number and unity Lewis number at Re_t=150, and at p=4bar. The contours represent the values of the moment of the area-weighted probability density with respect to the flame displacement speed. In order to investigate the sensitivity of the reference location on the flame displacement speed with

and without preferential diffusion, we compare the results at three different iso-surfaces with respect to progress variable defined in Eq. (12): c=0.3 (preheat zone), c=0.5 (reaction zone) and c=0.8 (fully-burned zone). Four observations can be made: first, Fig. 9 shows that the flame with non-unity Lewis number has a higher flame displacement speed than the flame with unity Lewis number at all three regions. This observation confirms that the flame acceleration is influenced by the preferential diffusion because the laminar flame speed is faster for the flame with non-unity Lewis number than the flame with unity Lewis number. It is also observed that the peak value of the flame displacement speed is increasing from preheat zone (c=0.3) to reaction zone (c=0.5) to fully burned zone (c=0.8) for the two cases. Second, the flame displacement speed shows a non-linear behaviour for the expanding spherical flame with non-unity Lewis number for all three reference locations. However, the non-linear behaviour is strongest in the preheat region. Interestingly, for the unity Lewis number case, the scattered data display a linear distribution for all three references iso-surfaces. The non-linear behavior of the flame displacement speed at higher stretch rate confirms that the displacement speed is influenced by the preferential diffusion. Third, the peak probability of the flame displacement speed occurs at higher stretch rate for the non-unity Lewis number case compared to the unity Lewis number case. For the flame with non-unity Lewis number, the JPDF of the flame displacement speed and stretch rate shows peak probability at approximately 2.0 m/s and at stretch rate of 50000 1/s in the reaction zone. However, for the flame with unity Lewis number, the JPDF shows peak probability at approximately 1.3 m/s and at stretch rate of 35000 1/s in the reaction zone. The high values of stretch rate associated with very high strain rate values exhibit for the flame with non-unity

Lewis number are a consequence of the positively curved crests that arise frequently on the flame surface as a result of preferential diffusion effects on flame stretch. Fourth, the gradients of the flame displacement speed curves (linear fit marked in solid lines) in Fig. 9 yield values of the turbulent Markstein lengths, which can be determined using an expression:

$$S_f = S_f^0 - L\mathrm{k} \tag{28}$$

where S_f is the local flame speed (in our case displacement speed), S_f^0 the unstretched flame speed, k the local stretch rate. The proportionality coefficient L is known as the Markstein length. In our study, Eq. (28) is defined based on velocities relative to the burned gas. A good linear fit was achieved between S_f and k and the unstretched flame speed, S_f^0, obtained by extrapolating the data to stretch rate $\mathrm{k} = 0$. The respective slope is defined as the Markstein length (L).

It is found that the slopes or the Markstein lengths L are negative for the selected flame positions and vary significantly depending on the flame reference location where the flame displacement speed was evaluated. Particularly, the variation in slopes for each reference progress variable iso-surface are found to be larger for non-unity Lewis number compared to unity Lewis number. For example, as illustrated in Fig. 9, for reference location inside the preheat zone (c=0.3), the respective slopes are found to be L = -0.024mm and L = -0.02mm for flames with non-unity Lewis number and unity Lewis number, respectively. However, for a reference location within the reaction zone (c=0.5), the respective slopes are found to be L = -0.05mm and L = -0.026mm for flames with non-unity and unity Lewis number, respectively. Furthermore, for a reference

location within the fully-burned zone (c=0.8), the respective slopes are found to be L = -0.08mm and L = -0.037mm for flames with non-unity and unity Lewis number, respectively.

3.4 Species Transport

To assess the preferential diffusion effects on chemical species diffusion under high turbulence and elevated pressure, we evaluate the local diffusive flow of fuel concentration along the flame front (i.e. c=0.5 or flame isotherm, T=1240K). For this we compare the H_2 transport along the flame front between the flame with non-unity Lewis number and the flame with unity Lewis number at Re_t=150, and at p=4bar. To characterise the diffusive flow of fuel transport, the equation of diffusion flux of fuel normal to the temperature gradient is used:

$$\vec{\Gamma}_{H_2}^{T} = \left[I - \frac{(-\lambda\nabla T)(-\lambda\nabla T)^{T}}{\left\|-\lambda\nabla T\right\|^{2}} \right] \vec{\Gamma}_{H_2}, \tag{29}$$

where $\vec{\Gamma}_{H_2}^{T}$ represents diffusion flux of H_2 and is equal to $-\rho D_{H_2}\nabla Y_{H_2}$, D_{H_2} is the mixture-averaged diffusivity of H_2 molecules, λ is the thermal conductivity and I is the unit matrix.

Shown in Fig. 10 (a1) and (b1) are flame isotherms coloured by the fraction of local H_2 diffusive flux for the flame with non-unity Lewis number and the flame with unity Lewis number at Re_t=150, and at p=4bar. The values of the fraction of local H_2 diffusive flux in the selected isotherm are found to increase near the edge of the cellular flame structures and then they decrease to zero in the middle part of the cell structures. In particular, the

fraction of local H_2 diffusive flux representing the flame with non-unity Lewis number show slightly longer structures compared to the flame with unity Lewis number. Results obtained for the non-dimensional divergence of the H_2 diffusive flow velocity for flames with non-unity and unity Lewis numbers are shown in Fig. 10 (a2) and (b2). The divergence of the H_2 diffusive flow velocity indicates pockets of higher values for the flame with non-unity Lewis number. On the other hand, the divergence field shows relatively small (close to zero) and largely uniform distribution for the flame with unity Lewis number. This confirms that preferential diffusion influences the divergence of the H_2 diffusive flow velocity at Re_t=150, and at p=4bar.

Having shown the influence of preferential diffusion on statistics of the local H_2 diffusive flux and the divergence of the H_2 diffusive flow velocity, it remains to analyse the statistical behaviour of the distribution of fuel (H_2) and air (O_2) together at Re_t=150, and at p=4bar. For this, we plotted the probability of the fraction of transport in isotherm for H_2 and O_2 over the surface. It is evident from Fig.10 (a3) and (b3) that the distributions of fuel (H_2) and air (O_2) collapse into one profile for the flame with unity Lewis number over most of the burning region. It is clear from Fig. 10 (a3) that the probability of fraction of transport in isotherm for H_2 and O_2 deviate from each other for the flame with non-unity Lewis number. This is a consequence of the preferential diffusion as H_2 as the more diffusive reactant is depleted faster than O_2 by diffusion in the fuel lean mixture for the flame with non-unity Lewis number.

4. Conclusions

The effects of preferential diffusion on cellular flame structure and propagation, onset of instabilities and chemical species diffusion transport in turbulent lean premixed high hydrogen content syngas flame at elevated pressure were numerical studied. Three-dimensional DNS with detailed chemistry and mixture-averaged transport model has been carried out for constant pressure expanding spherical flame configuration in the thin reaction zone regime. Simulations were performed for turbulent lean premixed H_2/CO syngas fuel mixture with 70% H_2 and 30% CO by volume with an equivalence ratio of 0.7. Data pertaining to the preferential diffusion effects on cellular flame structures, onset of instabilities, chemical species diffusion transport and flame speeds under low and high turbulence levels at elevated pressures were obtained.

The results show that the preferential diffusion effects play a significant role on forming small scale thermo-diffusive instability cells for lean premixed syngas flames which operate under conditions of low turbulence and elevated pressure. We also observed that the thermo-diffusive instability is overwhelmed by turbulent mixing for lean premixed syngas flames which operate under conditions of high turbulence and elevated pressure. It has been found that the flame acceleration is influenced by the preferential diffusion at elevated pressures. We observed higher flame acceleration for the flame with non-unity Lewis number compared to the flame with unity Lewis number under high turbulence and elevated pressure due to faster laminar flame speed as a result of preferential diffusion effects. The joint probability density function of flame displacement speed versus stretch revealed that preferential diffusion effects tend to produce higher displacement speed, strong non-linear behaviour and steep gradients or higher Markstein

lengths for the lean premixed syngas flame operates under high turbulence and elevated pressure conditions. The analysis of chemical species diffusion transport also revealed that preferential diffusion influences the local diffusive flow of hydrogen concentration under high turbulence and elevated pressure conditions.

Acknowledgements

This work was sponsored by the Engineering and Physical Sciences Research Council (EPSRC), under the grant EP/L025051/1 (High Hydrogen Content Fuel Burning at High Pressure). Computing resources on UK National Supercomputer ARCHER funded by the EPSRC grant No. EP/J016381/2 are gratefully acknowledged.

References

1. Ghoniem AF. Oxy-fuel combustion of pulverized coal: Characterization, fundamentals, stabilization and CFD modeling. Prog Energy Combust Sci 2012; 38: 156-214.

2. Wall TF. Combustion processes for carbon capture. Proc Combust Inst 2007; 31: 31-47.

3. Verhelst S, Wallner T. Hydrogen-fueled internal combustion engines. Prog Energy Combust Sci 2009; 35: 490-527.

4. Lieuwen T, Yang V, Yetter R. Synthesis Gas Combustion. CRS Press, Taylor and Francis Group, 2010.

5. Hu E, Huang Z, He, J, Miao, H. Experimental and numerical study on lean premixed methane-hydrogen-air flames at elevated pressures and temperature. Int J Hydrogen Energy 2009; 34: 6951-6960.

6. Vu TM, Park J, Kwon OB, Bae DS, Yun JH. Effects of diluents on cellular instabilities in outwardly propagating spherical syngas-air premixed flames. Int J Hydrogen Energy 2010; 35: 3868-3880.

7. Burke MP, Chaos M, Dryer FL, Ju Y. Negative pressure dependence of mass burning rates of H2/CO/O2/diluent flames at low flame temperatures. Combust Flame 2010; 157: 618-631.

8. Vu TM, Park J, Kim JS, Kwon OB, Yun JH, Keel SN. Experimental study of cellular instabilities in hydrocarbon/hydrogen/carbon monoxide-air premixed flames. Int J Hydrogen Energy 2011; 36: 6914-6924.

9. Liu F, Bao X, Gu J, Chen R. Onset of cellular instabilities in spherically propagating hydrogen-air premixed laminar flames. Int J Hydrogen Energy 2012; 37: 11458-11465.

10. Xie Y, Wang J, Xu N, Yu, S, Huang Z. Comparative study on the effect of CO_2 and H_2O dilution on laminar burning characteristics of CO/H_2/air mixtures. Int J Hydrogen Energy 2014; 39: 3450-3458.

11. Xie Y, Wang J, Xu N, Yu S, Zhang M, Huang Z. Thermal and chemical effects of water addition on laminar burning velocity of syngas. Energy and Fuels 2014; 28: 3391-3398.

12. Okafor EC, Nagano Y, Kitagawa T. Experimental and theoretical analysis of cellular instability in lean H_2-CH_4-air flames at elevated pressures. Int J Hydrogen Energy 2016; 41: 6581-6592.

13. Nilsson EJK, Konnov AA. Role of HOCO chemistry in syngas combustion. Energy and Fuels 2016 ; 30 :2443-2457.

14. Wang J, Xie Y, Cai X, Nie Y, Peng C, Huang Z. Effect of H2O addition on the flame front evolution of syngas spherical propagation flames. Combust Sci Technology 2016 ; 188 : 1054-1072.

15. Poinsot T, Candel S, Trouve A. Applications of direct numerical simulation to premixed turbulent combustion. Prog Energy Combust Sci 1995 ; 21 :531-576.

16. Westbrook CK, Mizobuchi Y, Poinsot TJ, Smith PJ, Warnatz J. Computational combustion. Proc Combust Inst 2005; 30: 125–157.

17. Chen JH. Petascale direct numerical simulation of turbulent combustion-fundamental insights towards predictive models. Proc Combust Inst 2011; 33: 99-123.

18. Matalon M. Intrinsic Flame Instabilities in Premixed and Nonpremixed Combustion. Annu Rev Fluid Mech 2007; 39: 163-191.

19. Im HG, Chen JH. Preferential diffusion effects on the burning rate of interacting turbulent premixed hydrogen-air flames. Combust Flame 2002; 131: 246-258.

20. Bell JB, Cheng RK, Day MS, Shepherd IG. Numerical simulation of Lewis number effects on lean premixed turbulent flames. Proc Combust Inst 2007; 31:1309-1317.

21. Bisetti F, Chen JY, Chen JH, Hawkes ER. Differential diffusion effects during the ignition of a thermally stratified premixed hydrogen-air mixture subject to turbulence. Proc Combust Inst 2009; 32: 1465-1472.

22. Dunstan TD, Jenkins KW. The effects of hydrogen substitution on turbulent premixed methane-air kernels using direct numerical simulation. Int J Hydrogen Energy 2009; 34: 8389-8404.

23. Vreman AW, van Oijen JA, de Goey LPH, Bastiaans RJM. Direct numerical simulation of hydrogen addition in turbulent premixed Bunsen flames using flamelet-generated manifold reduction. Int J Hydrogen Energy 2009; 34: 2778-2788.

24. Aspden AJ, Day MS, Bell JB. Lewis number effects in distributed flames. Proc Combust Inst 2011; 33:1473-1480.

25. Aspden AJ, Day MS, Bell JB. Characterization of low Lewis number flames. Proc Combust Inst 2011; 33.1463-1471.

26. Wang H, Luo K, Qiu K, Lu S, Fan J. A DNS study of hydrogen/air swirling premixed flames with different equivalence ratios. Int J Hydrogen Energy 2012; 37: 5246-5256.

27. Kim TH, Song WS, Park J, Kwon OB, Park JH. Effects of preferential diffusion on downstream interaction in premixed H_2/CO syngas-air flames. Int J Hydrogen Energy 2012; 37: 12015-12027.

28. Luo K, Wang H, Bushe WK, Fan J. Direct numerical simulation and reaction rate modelling of premixed turbulent flames. Int J Hydrogen Energy 2014; 39: 12158-12165.

29. Ranga Dinesh KKJ, Jiang X, van Oijen JA, Bastiaans RJM, de Goey LPH. Hydrogen-enriched nonpremixed jet flames: effects of preferential diffusion. Int J Hydrogen Energy 2013; 38: 4848-4863.

30. Ranga Dinesh KKJ, Jiang X, van Oijen JA. Hydrogen-enriched non-premixed jet flames: compositional structures with near-wall effects. Int J Hydrogen Energy 2013; 38: 5150-5164.

31. Ranga Dinesh KKJ, Jiang X, van Oijen JA. Hydrogen-enriched non-premixed jet flames: analysis of the flame surface, flame normal, flame index and Wobbe index. Int J Hydrogen Energy 2014; 39: 6753-6763.

32. Ranga Dinesh KKJ, van Oijen JA, Luo, KH, Jiang X. Nitric oxide pollutant formation in high hydrogen content (HHC) syngas flames. Int J Hydrogen Energy 2015; 40: 13621-13634.

33. Sun H, Yang SI, Jomaas G, Law CK. High-pressure laminar flame speeds and kinetic modeling of carbon monoxide/hydrogen combustion. Proc Combust Inst 2007; 31: 439–446.

34. Natarajan J, Kochar Y, Lieuwen T, Seitzman J. Pressure and preheat dependence of laminar flame speeds of H_2/CO/CO_2/O_2/He mixtures. Proc Combust Inst 2009; 32: 1261–1268.

35. Goswami M, Bastiaans RJM, Konnov AA, de Goey LPH. Laminar burning velocity of lean H_2-CO mixtures at elevated pressure using the heat flux method. Int J Hydrogen Energy 2014; 39: 1485-1498.

36. Goswami M, van Griensven JGH, Bastiaans RJM, Konnov AA, de Goey LPH. Experimental and modeling study of the effect of elevated pressure on lean high-hydrogen syngas flames. Proc Combust Inst 2015; 35: 655-662.

37. Law CK, Jomaas G, Bechtold JK. Cellular instabilities of expanding hydrogen/propane spherical flames at elevated pressures: theory and experiment. Proc Combust Inst 2005; 30: 159-167.

38. Bradley D, Lawes M, Liu K, Verhelst S, Woolley R. Laminar burning velocities of lean hydrogen-air mixtures at pressures up to 1.0 MPa. Combust Flame 2007; 149: 162-172.

39. Hilbert R, Thevenin D. Autoignition of turbulent non-premixed flames investigated using direct numerical simulations. Combust Flame 2002; 128: 22–37.

40. Hilbert R, Tap F, El-Rabii H, Thevenin D. Impact of detailed chemistry and transport models on turbulent combustion simulations. Prog Energy Combust Sci 2004; 30: 165–193.

41. Hirschfelder J, Curtiss C, Bird R. Molecular Theory of Gases and Liquids. Wiley, New York 1954.

42. Yoo CS, Im HG. Characteristic boundary conditions for simulations of compressible reacting flows with multi-dimensional, viscous and reaction effects. Combust Theory Model 2007; 11: 259-286.

43. Klein M, Sadiki A, Janicka J. A digital filter based generation of inflow data for spatially developing direct numerical or large eddy simulations. J Comput Phys 2003; 186: 652–665.

44. Kempf A, Klein M, Janicka J. Efficient generation of initial- and inflow-conditions for transient turbulent flows in arbitrary geometries. Flow Turb Combust 2005; 74:67–84.

45. Sun ZY, Li GX, Li HM, Zhai Y, Zhou ZH. Buoyant unstable behaviour of initially spherical lean hydrogen-air premixed flames. Energies 2014: 7: 4938-4956.

46. Bechtold JK, Matalon M. Hydrodynamic and diffusion effects on the stability of spherically expanding flames. Combust Flame 1987; 67: 77-90.

47. Bradley D, Harper CM. The development of instabilities in laminar explosion flames. Combust Flame 1994; 99: 562-572.

48. Bradley D. Instabilities and flame speeds in large-scale premixed gaseous explosions. Phil Trans R Soc Lond 1999; A 357: 3567-3581.

49. Savard B, Blanquart G. An a priori model for the effective species Lewis numbers in premixed turbulent flames. Combust Flame 2014; 161: 1547-1557.

50. Poinsot T, Veynante D. Theoretical Numerical Combustion. second ed., R.T. Edwards, Philadelphia, USA, 2005.

51. Giannakopoulos GK, Gatzoulis A, Frouzakis CE, Matalon M, Tomboulides AG. Consistent definitions of “Flame Displacement Speed” and “Markstein Length” for premixed flame propagation. Combust Flame 2015; 162: 1249-1264.

Table 1: Turbulence properties and parameter ranges at pressure value of p=4bar at the beginning of the simulation.

Case	**Flame A1**	**Flame A2**	**Flame B1**	**Flame B2**
Pressure (bar)	4 bar	4 bar	4 bar	4 bar
$\mathbf{Re_t}$[a]	15	15	150	150
Non-Unity Lewis number/Unity Lewis number	Unity Lewis number	Non-Unity Lewis number	Unity Lewis number	Non-Unity Lewis number
Da[b]	7.74	7.74	2.17	2.17
Ka[c]	0.51	0.51	5.63	5.63
ν $(\mathbf{m^2/s})$	4.13e-06	4.13e-06	4.13e-06	4.13e-06
$\mathbf{l_t}$**(m)**	6.37e-04	6.37e-04	6.37e-04	6.37e-04
$\mathbf{u'/S_L}$	0.6	0.6	3.2	3.2
$\mathbf{l_t/\delta_{th}}$	6.05	6.05	6.05	6.05
Grid Resolution	$600\times600\times600$	$600\times600\times600$	$600\times600\times600$	$600\times600\times600$
η $(\mu\mathbf{m})$[d]	8.3	8.3	14.9	14.9
$\Delta\mathbf{x}(\mu\mathbf{m})$ **(cell width)**	13	13	13	13
Number of grid points in flame thickness	8	8	8	8

u' - Root-mean-square (RMS) turbulent fluctuation velocity

l_t -Integral length scale measured directly from the initial turbulence field

ν - Kinematic viscosity

S_L -Laminar flame speed

[a]Turbulent Reynolds number, $Re_t = u' l_t / \nu$

[b]Damköhler number, $Da = \left(\frac{l_t}{u'} \right) \left(S_L / \delta_L \right)$

[c]Karlovitz number, $Ka = 15^{0.5} \left(\delta_{th} / S_L \right) \left(u' / \lambda \right)$

[d]Kolmogorov length scale, $\eta = l_t \, Re_t^{-0.75}$

λ - Taylor length scale, $\lambda = l_t \, Re_t^{-0.5}$

Figure Captions:

Fig.1. Working geometry of expanding turbulent spherical flame (iso-contours of temperature distribution at pressure p=4bar, and turbulent Reynolds number Re_t=150).

Fig. 2. (a) Temporal evolution of the integrated heat release rate; (b) spatial variation of the chemical production rate of hydrogen for four different grid resolutions ($200\times200\times200$, $400\times400\times400, 600\times600\times600$ and $800\times800\times800$) for the expanding spherical flame at turbulent Reynolds number of Re_t=150, and at pressure of p=4bar.

Fig.3. a: sequences of flame propagation, b: zoom view of section of the spherical flame showing that the development of cellular flame front instability with non-unity Lewis number and with unity Lewis number at turbulent Reynolds number of Re_t=15, and at pressure of p=4bar.

Fig.4. a: sequences of flame propagation, b: zoom view of section of the spherical flame showing that the development of cellular flame front instability for the expanding spherical flame with non-unity Lewis number and with unity Lewis number at turbulent Reynolds number of Re_t=150, and at pressure of p=4bar.

Fig. 5. Iso-surfaces of flame front (c=0.5), coloured by local curvature for the expanding spherical flame with non-unity Lewis number and with unity Lewis number at turbulent Reynolds number of Re_t=15 and 150 at pressure of p=4bar.

Fig. 6. Temporal evolution of the flame surface area and the flame radius for the expanding spherical flame with non-unity Lewis number and with unity Lewis number at turbulent Reynolds number of Re_t=15 and 150, and at pressure of p=4bar.

Fig.7. Darrieus-Landau (DL) instability, ω ,thermo-diffusive (TD) instability, $-\omega\Omega/Pe$, and growth rate, $\omega(1-\Omega/Pe)$ as a function of wave number for the expanding spherical flame with non-unity Lewis number and with unity Lewis number at turbulent Reynolds number of Re_t=15, and at pressure of p=4bar: $\sigma = 6.8$, $Pe = 303$, $\beta = 8.0$ and $Le_{eff} = 0.61$.

Fig.8. Darrieus-Landau (DL) instability, ω ,thermo-diffusive (TD) instability, $-\omega\Omega/Pe$, and growth rate, $\omega(1-\Omega/Pe)$ as a function of wave number for the expanding spherical flame with non-unity Lewis number and with unity Lewis number at turbulent Reynolds number of Re_t=150, and at pressure of p=4bar: $\sigma = 6.8$, $Pe = 435$, $\beta = 8.0$, $Le_{eff} = 0.91$.

Fig.9. Joint probability density function of flame displacement speed and stretch rate (1/s) for three selected progress variable iso-surfaces: c=0.3 (preheat region), c=0.5 (flame front), c=0.8 (fully burned region) for the expanding spherical flame with non-unity Lewis number and with unity Lewis number at turbulent Reynolds number of Re_t=150 and at pressure of p=4bar at an instantaneous time of 1.3e-4s.

Fig. 10. Iso-surfaces of flame front (c=0.5), coloured by (a1, b1) the fraction of local H_2 diffusive flow in the c=0.5 iso-surface, (a2, b2) the divergence of the normalised H_2 diffusive flow velocity in the c=0.5 iso-surface, and (a3, b3) distribution of the in-flame transport for H_2 and O_2 for the expanding spherical flame with non-unity Lewis number and with unity Lewis number at turbulent Reynolds number of Re_t=150 and at pressure of p=4bar at an instantaneous time of 1.3e-4s.

Figures:

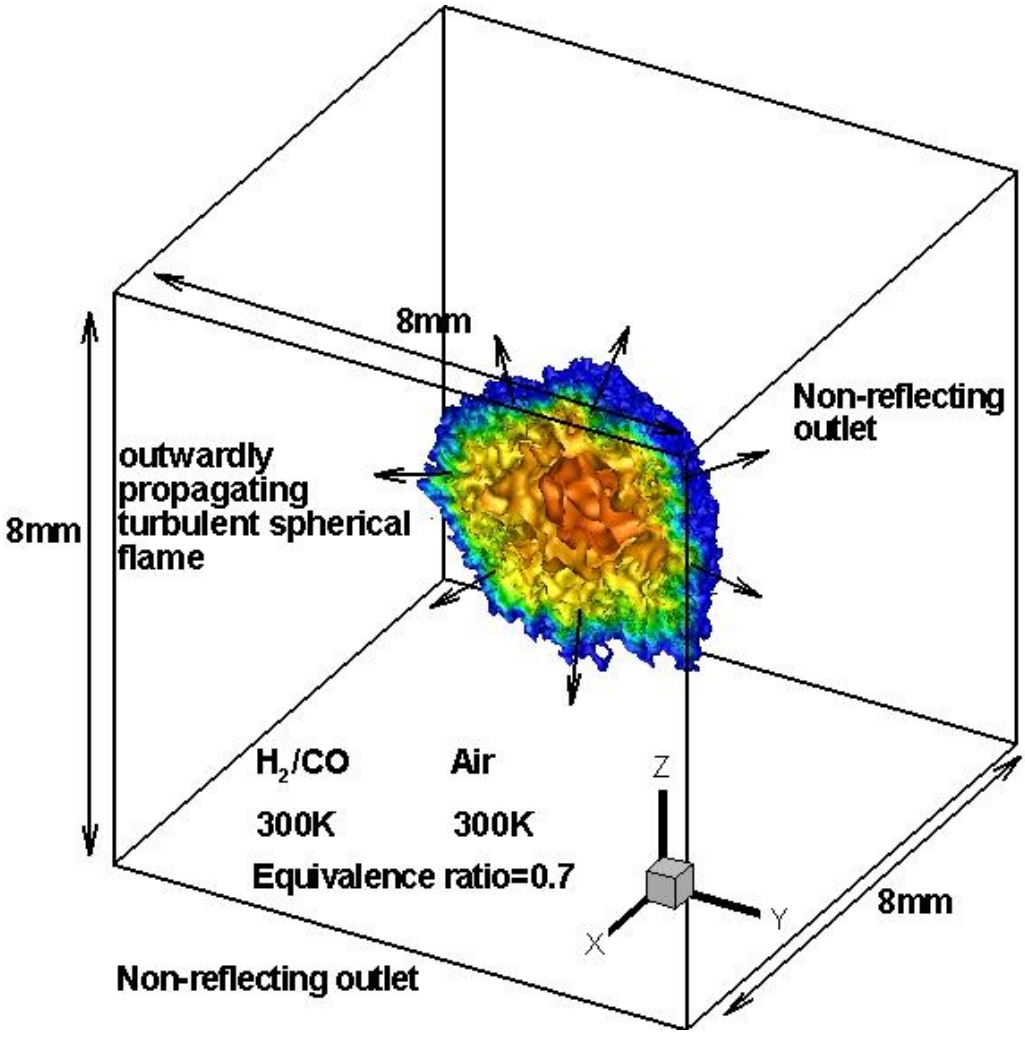

Fig.1. Working geometry of expanding turbulent spherical flame (iso-contours of temperature distribution at pressure p=4bar, and turbulent Reynolds number Re_t=150).

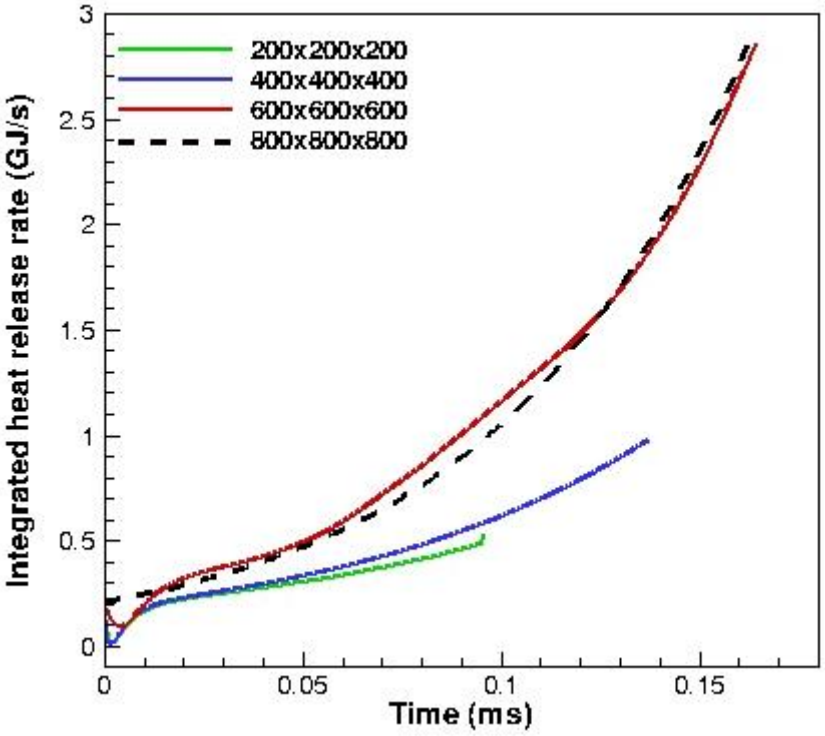
200x200x200
400x400x400
600x600x600
800x800x800
Integrated heat release rate (GJ/s)
Time (ms)
0
0.5
1
1.5
2
2.5
3
0
0.05
0.1
0.15

(a)

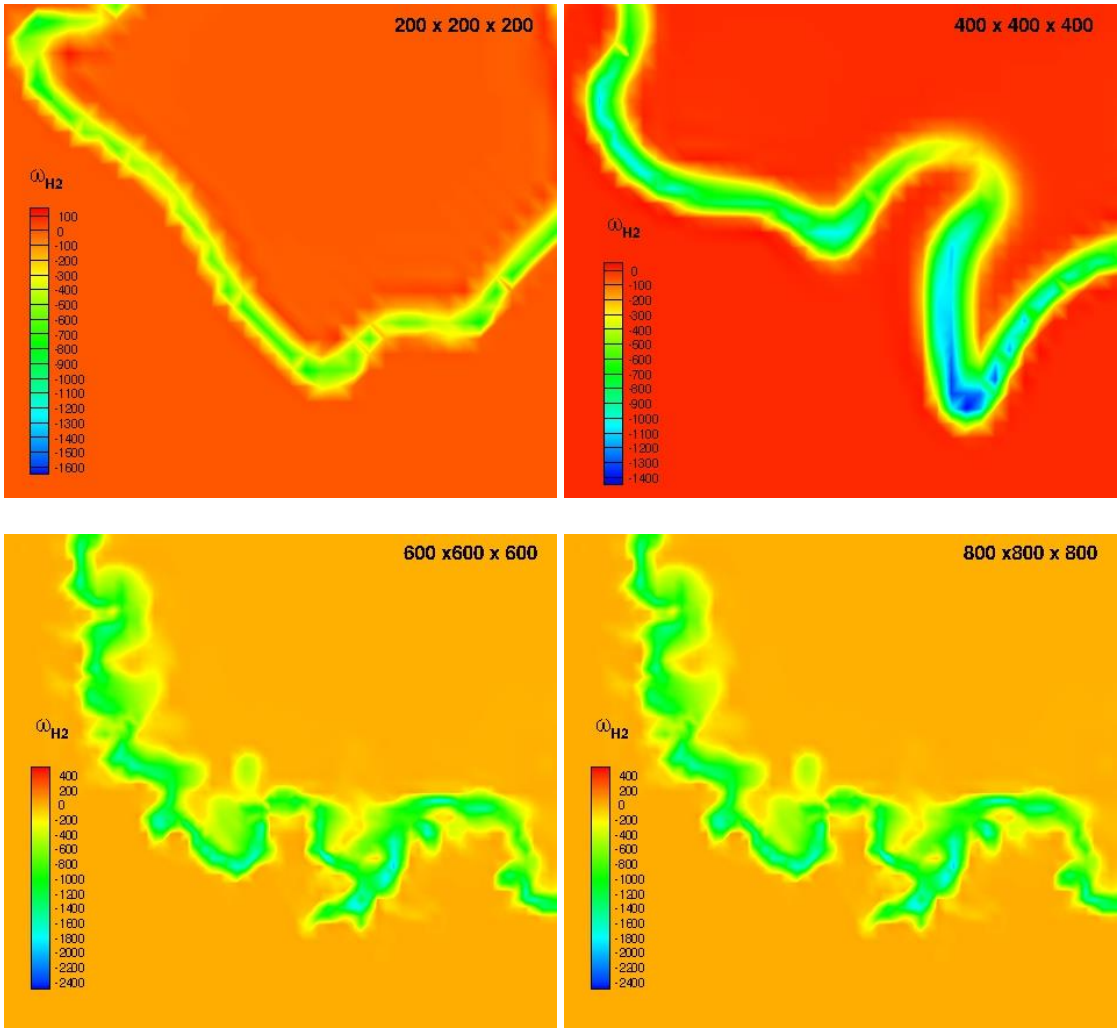

(b)

Fig. 2. (a) Temporal evolution of the integrated heat release rate; (b) spatial variation of the chemical production rate of hydrogen for four different grid resolutions ($200\times200\times200$, $400\times400\times400$, $600\times600\times600$ and $800\times800\times800$) for the expanding spherical flame at turbulent Reynolds number of Re_t=150, and at pressure of p=4bar.

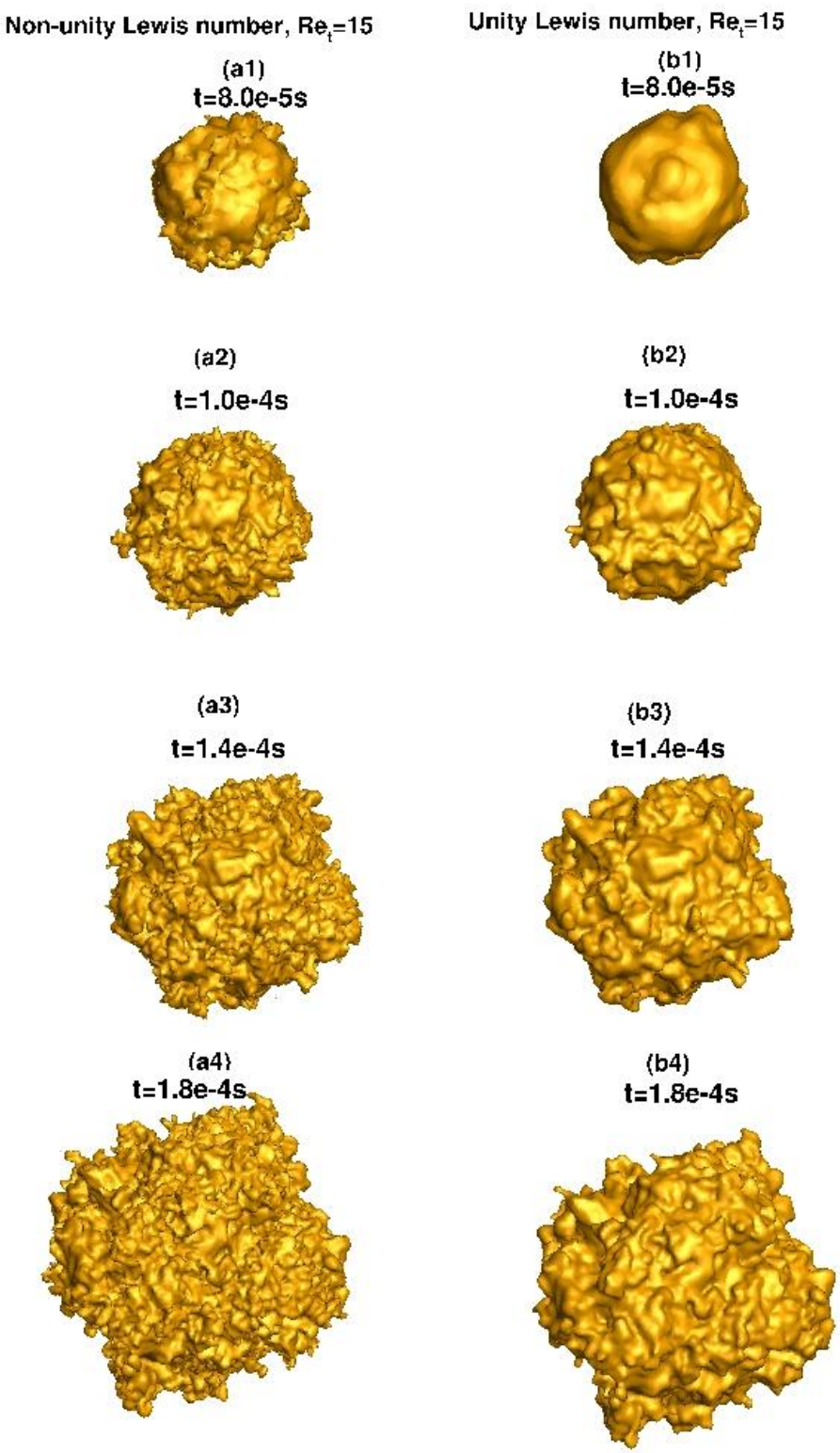
Non-unity Lewis number, Re$_t$=15
Unity Lewis number, Re$_t$=15
(a1)
t=8.0e-5s
(b1)
t=8.0e-5s
(a2)
t=1.0e-4s
(b2)
t=1.0e-4s
(a3)
t=1.4e-4s
(b3)
t=1.4e-4s
(a4)
t=1.8e-4s
(b4)
t=1.8e-4s

(a)

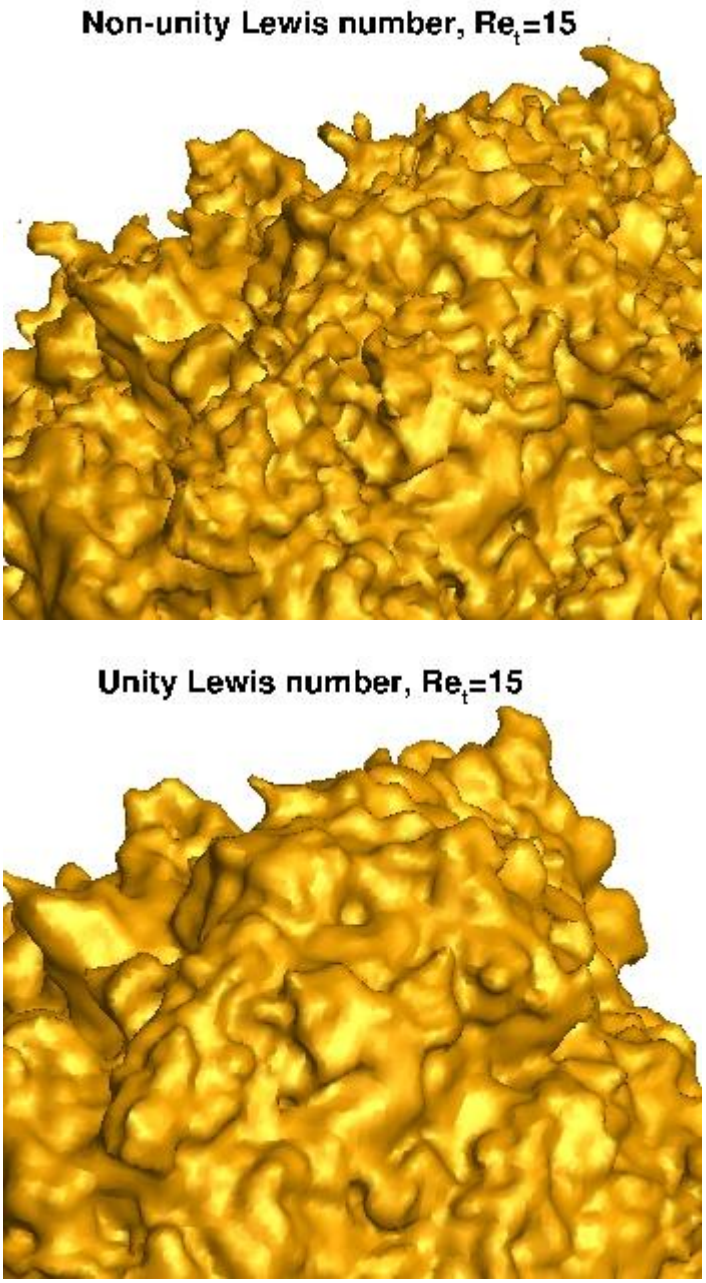

(b)

Fig.3. a: sequences of flame propagation, b: zoom view of section of the spherical flame showing that the development of cellular flame front instability with non-unity Lewis number and with unity Lewis number at turbulent Reynolds number of Re_t=15, and at pressure of p=4bar.

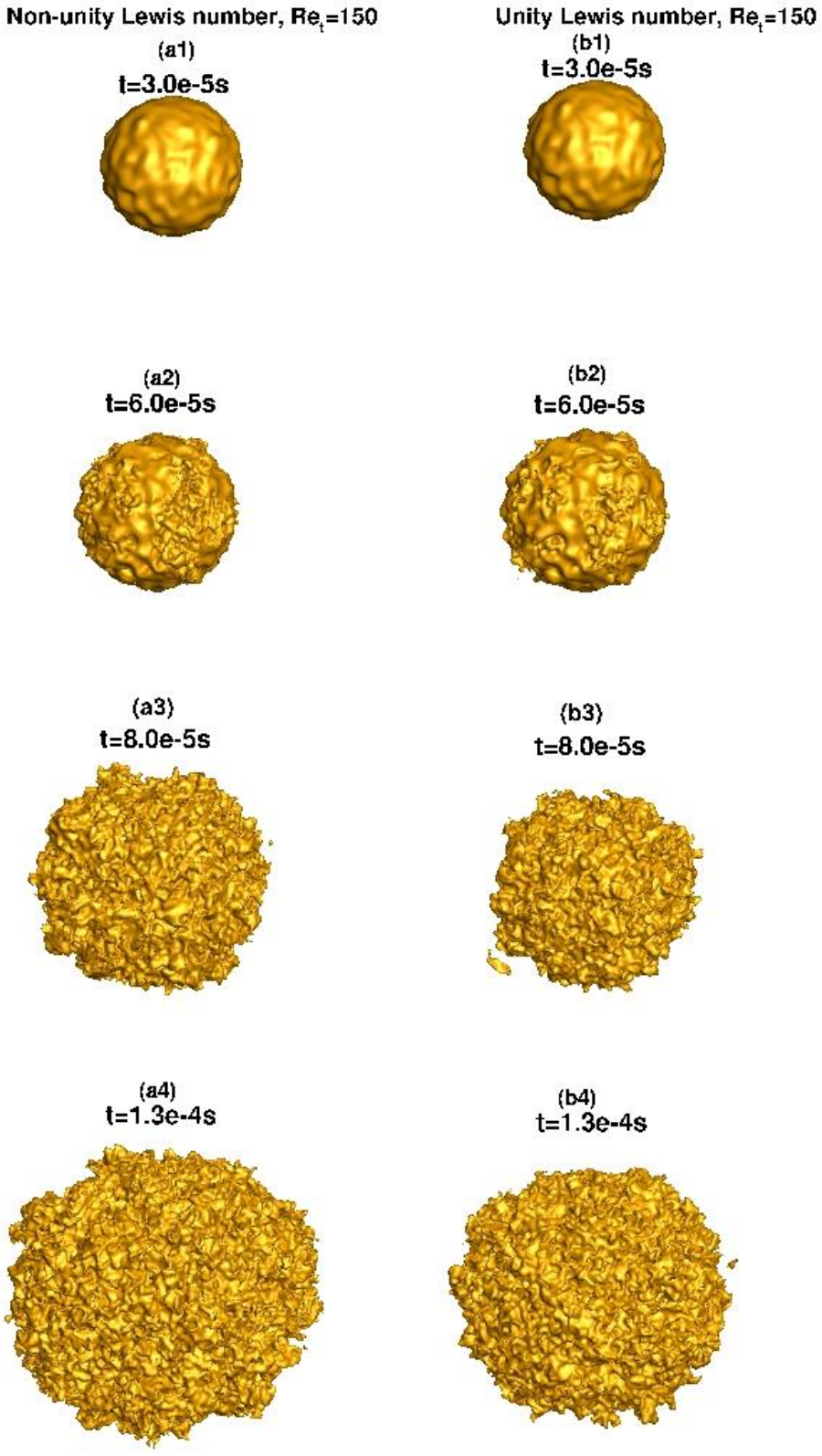
Non-unity Lewis number, Re$_t$=150
(a1)
t=3.0e-5s
Unity Lewis number, Re$_t$=150
(b1)
t=3.0e-5s
(a2)
t=6.0e-5s
(b2)
t=6.0e-5s
(a3)
t=8.0e-5s
(b3)
t=8.0e-5s
(a4)
t=1.3e-4s
(b4)
t=1.3e-4s

(a)

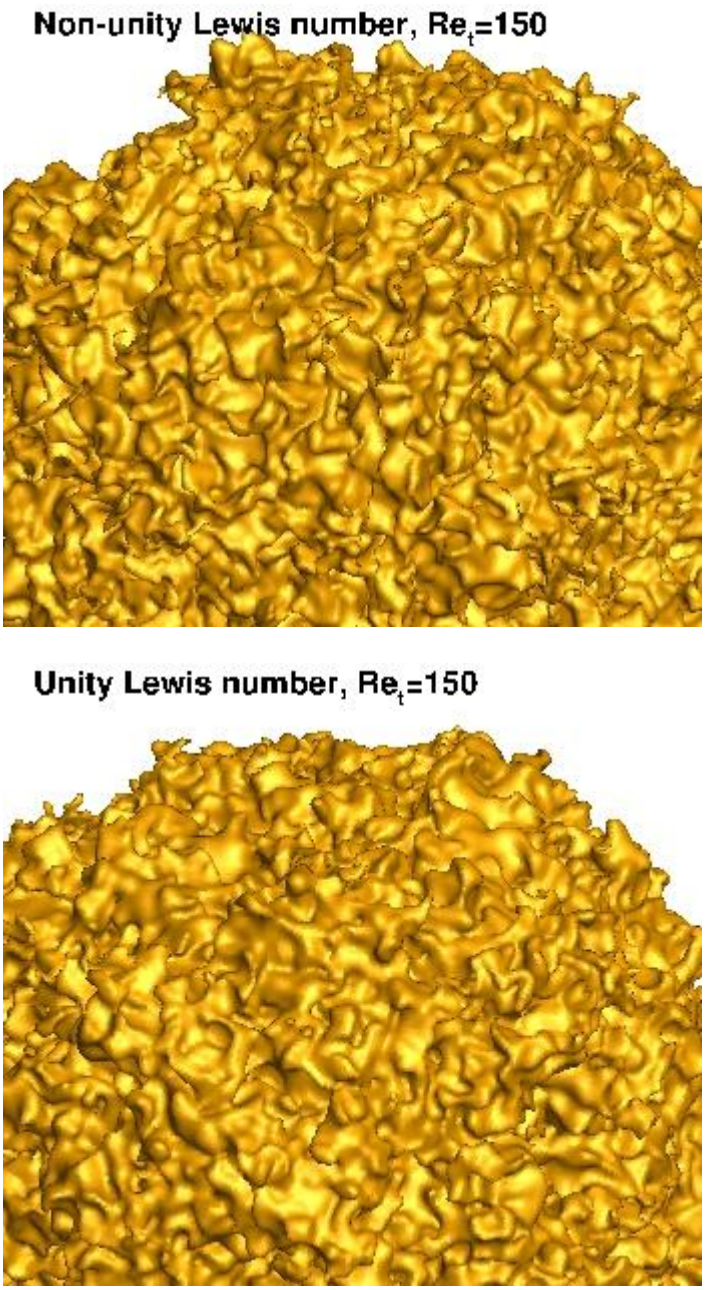

(b)

Fig.4. a: sequences of flame propagation, b: zoom view of section of the spherical flame showing that the development of cellular flame front instability for the expanding spherical flame with non-unity Lewis number and with unity Lewis number at turbulent Reynolds number of Re_t=150, and at pressure of p=4bar.

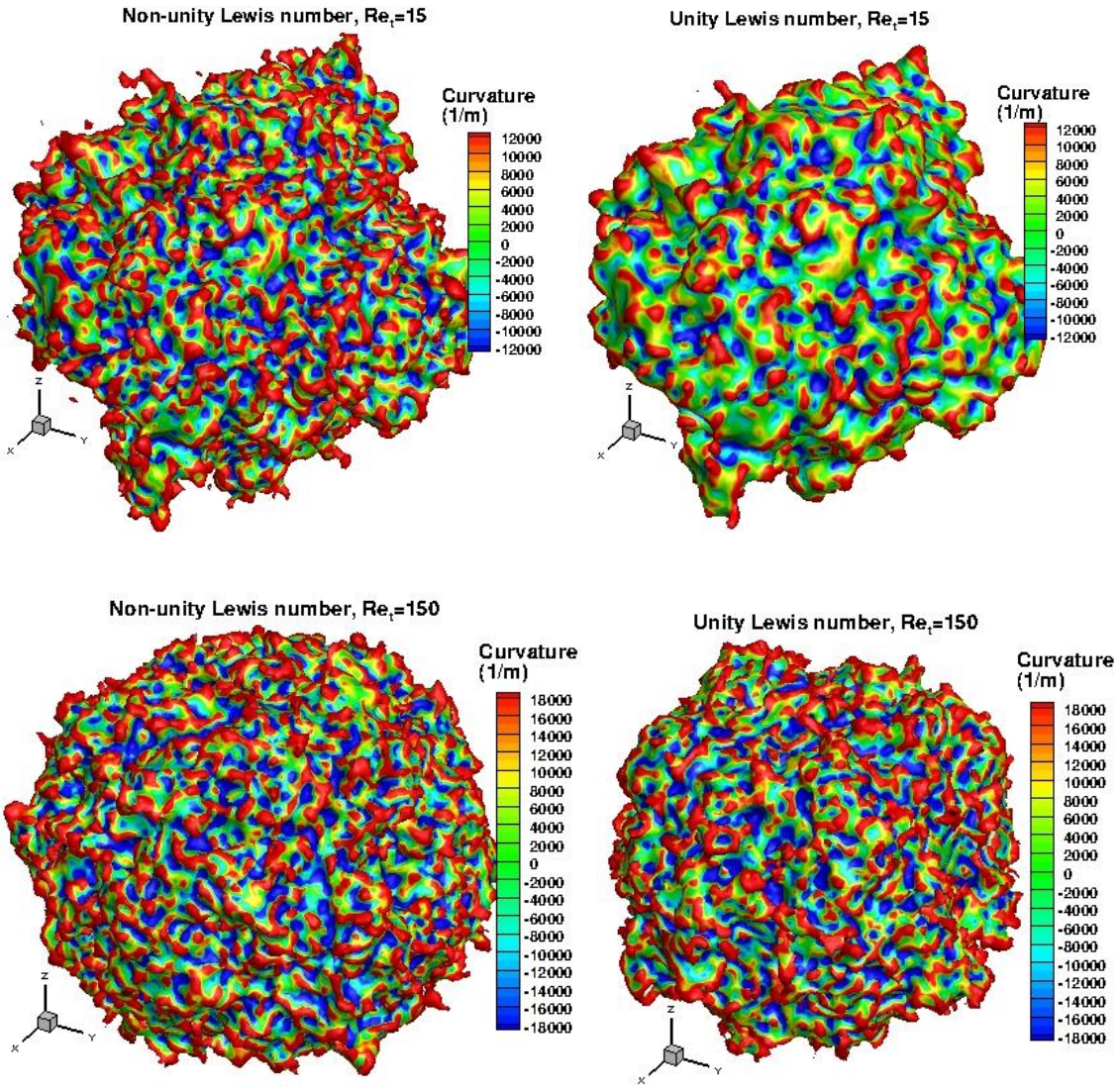

Fig. 5. Iso-surfaces of flame front (c=0.5), coloured by local curvature for the expanding spherical flame with non-unity Lewis number and with unity Lewis number at turbulent Reynolds number of Re_t=15 and 150 at pressure of p=4bar.

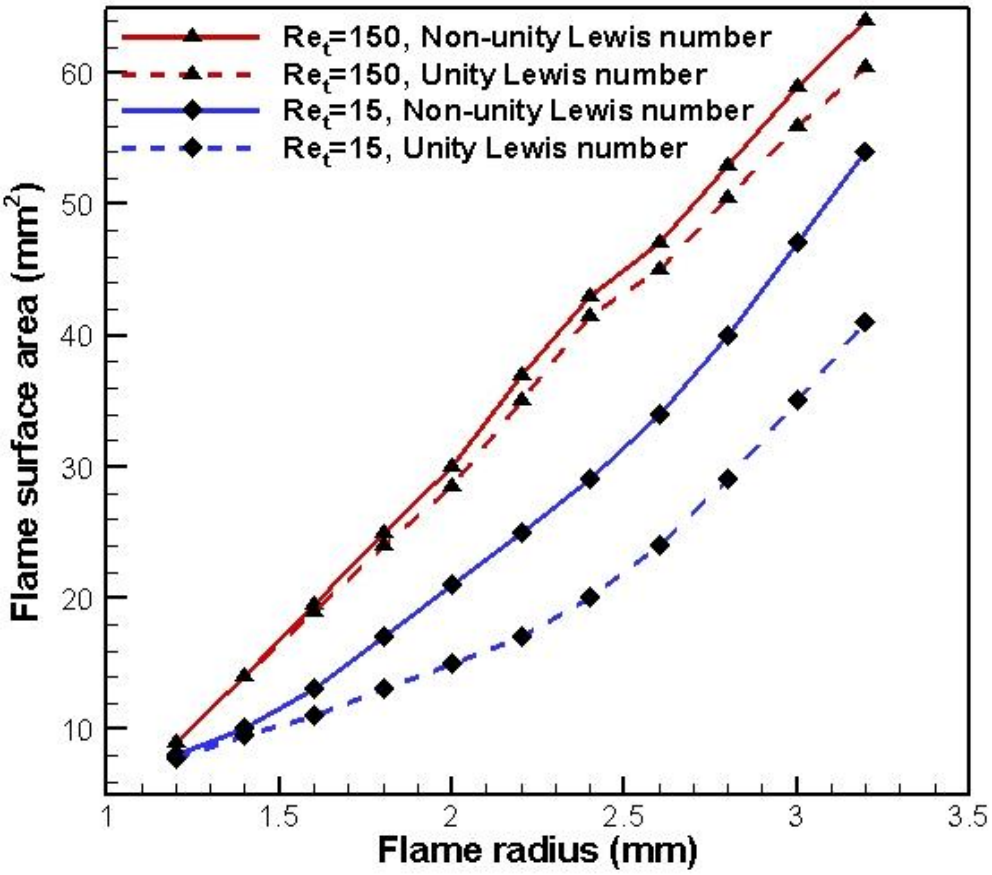

Fig. 6. Temporal evolution of the flame surface area and the flame radius for the expanding spherical flame with non-unity Lewis number and with unity Lewis number at turbulent Reynolds number of Re_t=15 and 150, and at pressure of p=4bar.

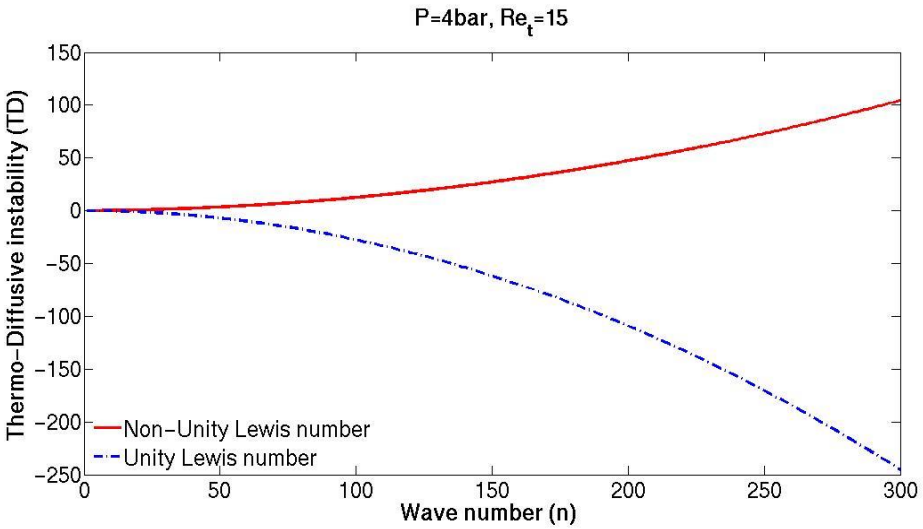
P=4bar, Re$_t$=15
Thermo-Diffusive instability (TD)
Wave number (n)
Non-Unity Lewis number
Unity Lewis number

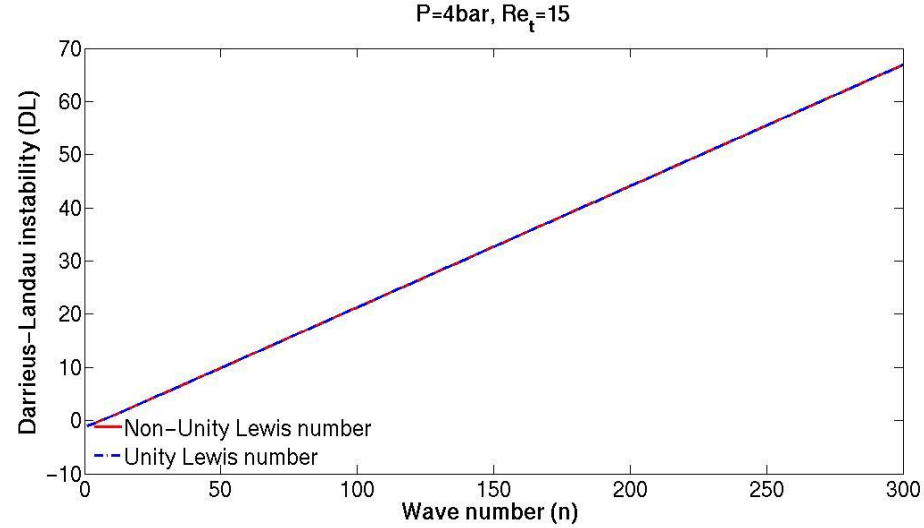
P=4bar, Re$_t$=15
Darrieus-Landau instability (DL)
Wave number (n)
Non-Unity Lewis number
Unity Lewis number

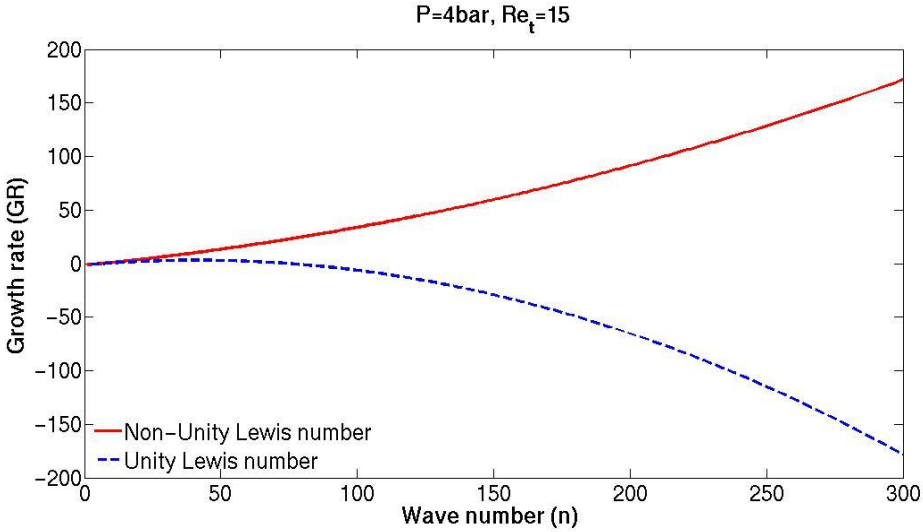
P=4bar, Re$_t$=15
Growth rate (GR)
Wave number (n)
Non-Unity Lewis number
Unity Lewis number

Fig.7. Darrieus-Landau (DL) instability, ω ,thermo-diffusive (TD) instability, $-\omega\Omega/Pe$, and growth rate, $\omega(1-\Omega/Pe)$ as a function of wave number for the expanding spherical flame with non-unity Lewis number and with unity Lewis number at turbulent Reynolds number of Re_t=15, and at pressure of p=4bar: $\sigma = 6.8$, $Pe = 303$, $\beta = 8.0$ and $Le_{eff} = 0.61$.

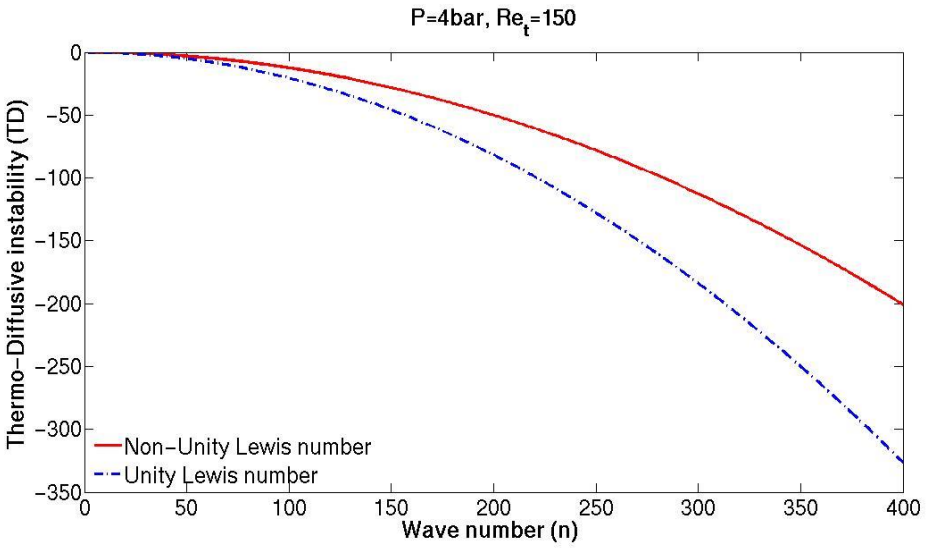
P=4bar, Re$_t$=150
Thermo−Diffusive instability (TD)
Wave number (n)
Non−Unity Lewis number
Unity Lewis number

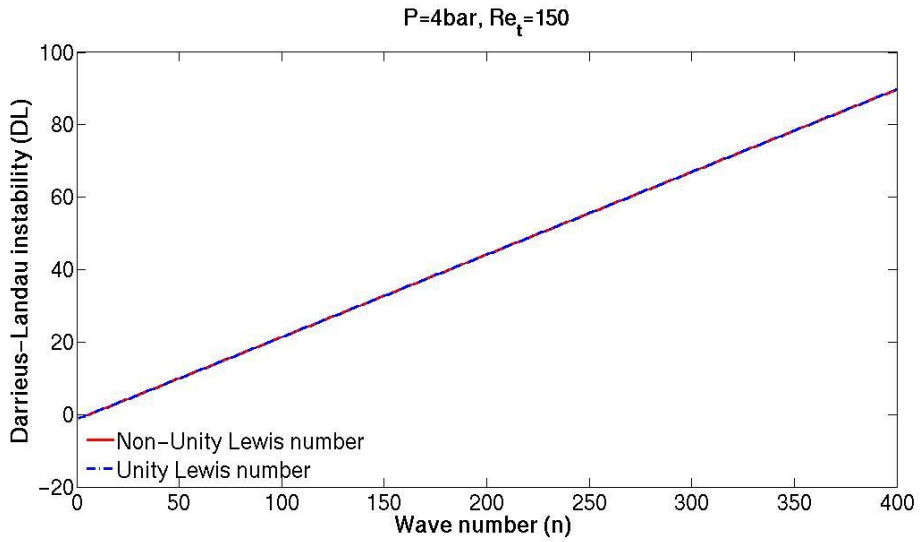
P=4bar, Re$_t$=150
Darrieus−Landau instability (DL)
Wave number (n)
Non−Unity Lewis number
Unity Lewis number

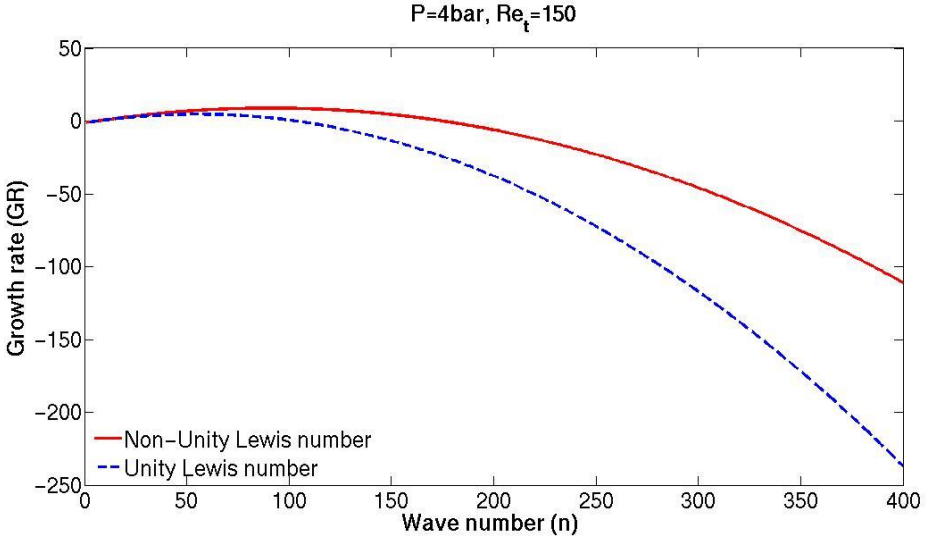
P=4bar, Re$_t$=150
Growth rate (GR)
Wave number (n)
Non−Unity Lewis number
Unity Lewis number

Fig.8. Darrieus-Landau (DL) instability, ω ,thermo-diffusive (TD) instability, $-\omega\Omega/Pe$, and growth rate, $\omega(1-\Omega/Pe)$ as a function of wave number for the expanding spherical flame with non-unity Lewis number and with unity Lewis number at turbulent Reynolds number of Re_t=150, and at pressure of p=4bar: $\sigma = 6.8$, $Pe = 435$, $\beta = 8.0$, $Le_{eff} = 0.91$.

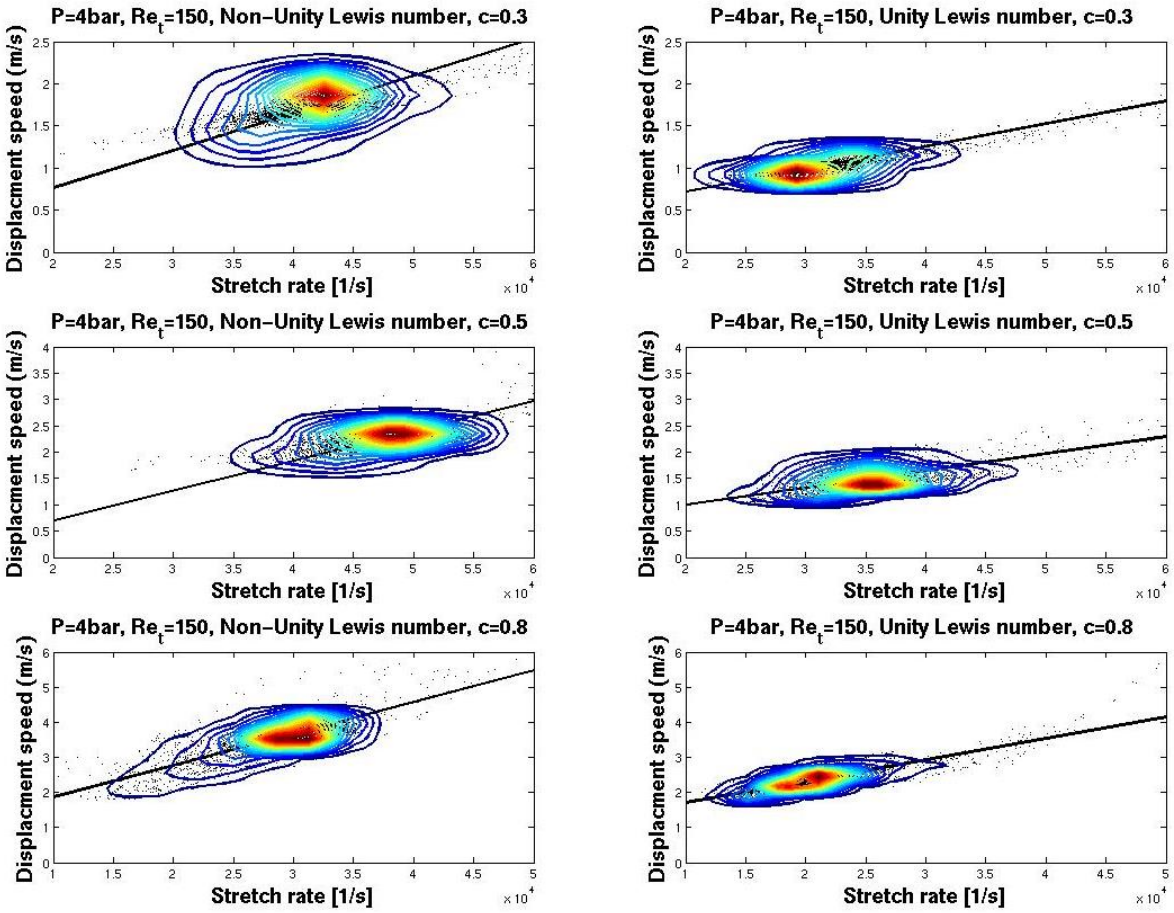

Fig.9. Joint probability density function of flame displacement speed and stretch rate (1/s) for three selected progress variable iso-surfaces: c=0.3 (preheat region), c=0.5 (flame front), c=0.8 (fully burned region) for the expanding spherical flame with non-unity Lewis number and with unity Lewis number at turbulent Reynolds number of Re_t=150 and at pressure of p=4bar at an instantaneous time of 1.3e-4s.

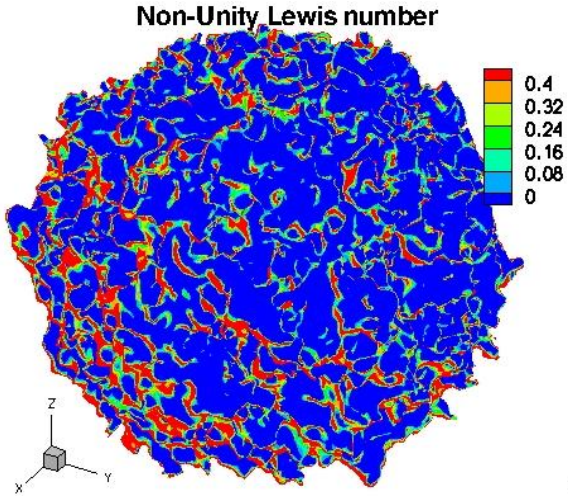

(a1)

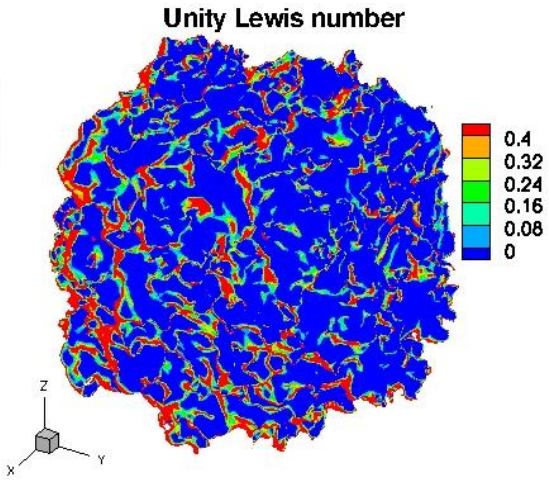

(b1)

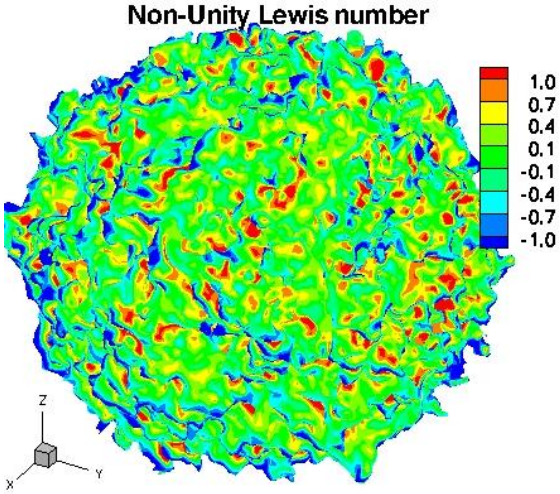

(a2)

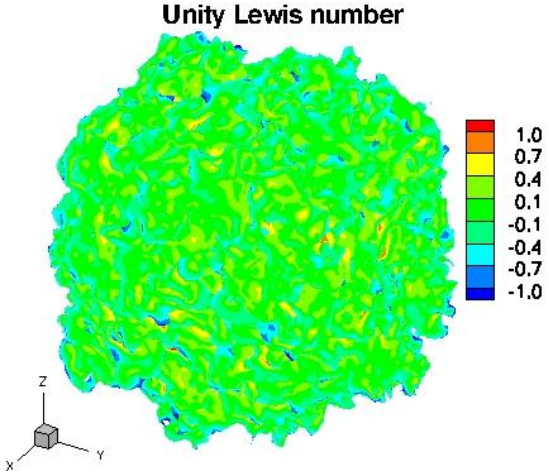

(b2)

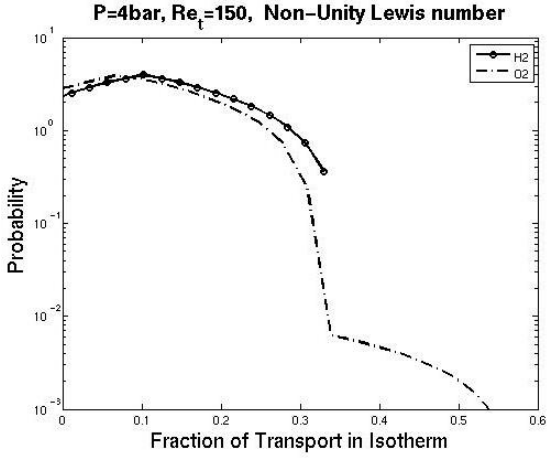

(a3)

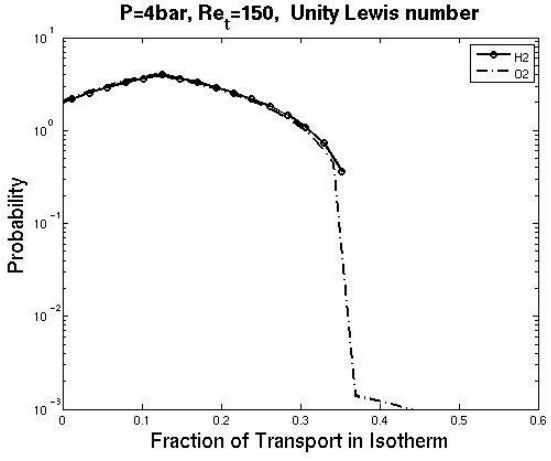

(b3)

Fig. 10. Iso-surfaces of flame front (c=0.5), coloured by (a1, b1) the fraction of local H_2 diffusive flow in the c=0.5 iso-surface, (a2, b2) the divergence of the normalised H_2 diffusive flow velocity in the c=0.5 iso-surface, and (a3, b3) distribution of the in-flame transport for H_2 and O_2 for the expanding spherical flame with non-unity Lewis number and with unity Lewis number at turbulent Reynolds number of Re_t=150 and at pressure of p=4bar at an instantaneous time of 1.3e-4s.